A Near Infrared Femtosecond Laser Source for Observation of Charge Transfer Processes in Semiconductors

by

Essraa Taha Mirghani Ahmed

Thesis presented in partial fulfilment of the requirements for the degree of Master of Science in Laser Physics in the Department of Physics at Stellenbosch University

Supervisor: Prof. Heinrich Schwoerer

Co-supervisor: Prof. Erich Rohwer
Laser Research Institute
Department of Physics
Stellenbosch University

March 2017

Declaration

By submitting this thesis electronically, I declare that the entirety of the work contained therein is my own, original work, that I am the sole author thereof (save to the extent explicitly otherwise stated), that reproduction and publication thereof by Stellenbosch University will not infringe any third party rights and that I have not previously in its entirety or in part submitted it for obtaining any qualification.

Date: ..... March 2017 .....

Abstract

A Near Infrared Femtosecond Laser Source for Observation of Charge Transfer Processes in Semiconductors

E.T.M. Ahmed

Department of Physics,
University of Stellenbosch,
Private Bag X1, Matieland 7602, South Africa.

Thesis: MSc

March 2017

Near infrared femtosecond laser pulses were generated in the spectral range 900 - 2400 nm using the idler of a noncollinear optical parametric amplifier (NOPA). The amplitude and phase of four exemplary pulses were retrieved using frequency resolved optical gating (XFROG). The durations of these pulses were found to be $\leq$ 151 fs. The generated pulses were used as a probe to detect the charge dynamics within two types of organic solar cells: indoline DN216/ZnO dye sensitized solar cell (DSSC) and fluorinated Zinc Phthalocyanine F_nZnPc/C_{60} ($n = 0, 4, 8, 16$) bilayer photovoltaic cell. The two organic cells utilize organic materials as light absorbers. In the DN216/ZnO DSSC, electrons are injected from the dye, the electron donor, into the conduction band of the inorganic semiconductor ZnO upon photoexcitation. The injection into the conduction band of ZnO was found to occur directly in 200 fs, via a neutral charge transfer state (NCT) in 2 ps or via an ionic charge transfer state (ICT) in 10 ps [1]. In the F_nZnPc/C_{60} ($n = 0, 4, 8, 16$) cells, electrons are injected into the C_{60} layer after dissociation of excitons at the donor/acceptor heterojunction [2]. A C_{60}^- anion is formed due to injection of electrons into the C_{60} layer as well as by direct photoexcitation of the molecule. The C_{60}^- formation was found to occur instantaneously after photoexcitation of either the donor or the acceptor material, independent of the energetics at the donor/acceptor heterojunction. Charge recombinations of the C_{60}^- anion within the F_nZnPc/C_{60}, $n = 0, 4, 8, 16$ cells were found to occur in the bulk of the C_{60} layer in 4 ps $\pm$ 1 ps as well as at the surface of the C_{60} layer with air in 43 ps $\pm$ 9 ps.

Uittreksel

'n Femtosekonde laser bron naby die infrarooi vir die waarneming van lading oordrag prosesse in halfgeleiers

("A Near Infrared Femtosecond Laser Source for Observation of Charge Transfer Processes in Semiconductors")

E.T.M. Ahmed

Departement Fisika,
Universiteit van Stellenbosch,
Privaatsak X1, Matieland 7602, Suid Afrika.

Tesis: MSc

Maart 2017

Naby-infrarooi-femtosekonde laser pulse, in die spektrale gebied 900-2400 nm, is gegenereer met 'n nie-saamlynige parametriese optiese versterker deur gebruik te maak van die tweede uitset sein. Die amplitude en fase van vier stelle pulse is gemeet deur gebruik te maak van frekwensie analiese optiese monster metode (XFROG). Die durasie van die pulse was ≤ 151 fs. Die gegenereerde pulse is aangewend om die ladings dinamika te ondersoek van twee tipes organiese son selle: indolien DN216/ZnO kleursel-gesensiteerde-son-sel (DSSC) en gefloorineerde sink Phthalocyanine FnZnPc/C_{60} ($n = 0, 4, 8, 16$) dubbel-laag fotovoltaisesel. Die twee organiese selle maak gebruik van die organiese materiaale om lig te absorbeer. In die DN216/ZnO DSSC word elektrone gedoneer vanaf die kleursel, die elektron donor, en oorgedra aan die geleidende-band van die anorganiese semi-geleier ZnO waneer foto-opwekking plaas vind. Dit is bevind dat die elektron-oordrag na die geleidings-band van die anorganiese half-geleier ZnO plaas vind in 200fs, die oordrag vind plaas via die neutrale ladings oordrags toestand (NCT) in 2 ps of langs 'n ioniese ladings oordrags toestand (ICT) in 10 ps [1]. In die geval van FnZnPc/C_{60} ($n = 0, 4, 8, 16$) selle word elektrone oorgedra na die C_{60} vlak na dissosiasie van eksitone by die donor/akseptor intervlak [2]. 'n C_{60}^{-} anioon word gevorm weens die oordrag van elektrone na die C60 laag sowel as deur direkte foto-opwekking van die molekule. Dit is bevind dat die C60 formasie oombliklik plaas vind na foto-opwekking van enige van die donor of die akseptor materiaal, onafhanklik van die energie toestande by die donor/akseptor hetero-intervlak. Daar is bevind dat, ladings herkombinasie in die F_nZnPc/C_{60}, $n = 0, 4, 8, 16$ selle plaas vind in die bulk van die C60 laag in 4 ps ± 1 ps sowel as by die intervlak van die oppervlak van die C60 laag en lug in 43 ps $\pm$ 9ps.

Acknowledgements

I would like to express my sincere gratitude to my supervisor Professor Heinrich Schwoerer for offering me the opportunity to join his research group, for his patience and continuous guidance throughout this project and for sharing his passion for experimental physics with me. Also, my gratitude extend to Iulia Minda and Dr. Michael Brendel not only for allowing me to take part in their phd projects but also for always finding the time to answer my many questions.

I would like to extend my gratitude to Dr. Dirk Spangenberg for helping me with the translation of this thesis abstract to Afrikaans. To Xavier von Stein for all your computer and software help. Thank you Dr. Nicholas Hale for the beautiful cover picture. Thank you Nancy Payne and Bart Smit for creating such a happy work environment and for being true friends.

I would also like to gratefully acknowledge the African Institute for Mathematical Sciences (AIMS - South Africa) for their financial support.

Thanks to my family for their love and support. Finally, thank you Taha Mirghani Ahmed, my father, for believing in my at times when I couldn't believe in my self.

Contents

Nomenclature

List of Abbreviations

BBO Beta Barrium Borate.
DSSC Dye Sensitized Solar Cells.
ESA Excited State Absorption.
FWHM Full Width at Half Maximum.
GSB Ground State Bleach.
HOMO Highest Occupied Molecular Orbital.
ICT Ionic Charge Transfer.
ITO Indium Tin Oxide.
LUMO Lowest Occupied Molecular Orbital.
NCT Neutral Charge Transfer.
NOPA Noncollinear Optical Parametric Amplifier.
OPA Optical Parametric Amplification.
OPVC Organic Photovoltaic Cells.
PHJ Planar Heterojunction Devices.
SHG Second Harmonic Generation.
TA Transient Absorption.
TAS Transient Absorption Spectroscopy.
WLG White Light Generation.
XFROG Cross-correlation Frequency Resolved Optical Gating.
YAG Yttrium Aluminium Garnet.

1. Introduction

From smart phones to huge data centres, we live in a world shaped by information and communication technologies. Google, the information technology company that runs the world's most popular search engine, was facing the accusation that a single typical Google search consumes "half as much energy as boiling a kettle of water" to make a cup of tea. Although Google denied these claims, explaining that they insure minimal energy consumption per search by using "energy efficient data centres", the company acknowledged that the increasing dependence on their search engine meant an increasing energy consumption [3]. This incident reflected the public concern about the increasing energy consumption of personal electronic devices (laptops, tablets, computers, etc..) as well as the consumption of data centres and telecommunication networks. Electronic devices gain popularity as they improve in computational power and the telecommunication networks connecting them are expanding as a result of the increasing number of users who have access to these devices. The increasing information and communication related energy consumption is only one element in a list of energy demanding elements related to human life style that includes others like transport, residential and industrial consumptions. The need for sustainable energy resources to supply the energy demands is now a public as well as a scientific concern.

The increasing energy demands and the availability of radiance from the sun has always been scientists' motivation to develop the solar energy-harvesting devices known as photovoltaic cells. Silicon based photovoltaic cells are the solar technology currently dominating the photovoltaics' market due to their high efficiency and long life. A crystalline silicon solar cell made by Panasonic, for example, has a recently recorded efficiency of 25.6%[4; 5]. However, organic photovoltaic cells (OPVCs) are an emerging solar cell technology that is often presented by researchers as a low cost alternative to the conventional silicon based solar cells. The term OPVCs refers to the family of photovoltaic cells which have at least one organic photoactive component [6]. This component could be the light absorber such as in organic and dye sensitized solar cells or the semiconductor such as in hybrid solar cells. OPVCs have many valuable properties such as flexibility and light weight and have a range of applications related to electronics, constructions and health care[7]. However, the low efficiency and stability of these alternative solar cells weaken them in the competition against the more dominant silicon based solar cells [8]. A precise understanding of the working principles of these solar cells on a microscopic scale is the key to transform them into long-living efficient energy harvesting devices.

The process of converting light into electrical current in organic photovoltaics [9; 8; 10] involves three main steps. The first of which is the absorption of photons and the consequent creation of the electronically excited molecule; a strongly bound electron-hole pair known as an exciton. The second step is exciton dissociation and the separation of charge. The separation occurs either via the injection of the charge into an acceptor in direct contact with the surface of the light absorber such as in dye sensitized solar

cells or after the exciton diffusion into a donor/acceptor interface such as in organic solar cells. The final step is the extraction of free charge carriers to the external circuit.

The contribution of the photoexcited molecules in OPVCs to the extracted photocurrent is limited by the losses due to inefficient light absorption, charge collection at the electrodes or recombination of excitons. Moreover, the energy deposited upon light absorption is localized in a small volume of few atoms and the photoexcited molecule will be forced to equilibrate with its surrounding. Energy relaxation processes in molecular systems occur on time scales down to 10^{-12} s. Therefore, the exciton generation, charge separation and extraction processes must all take place on a pico- to femtosecond time scale to overcome the losses for optimum production of the photocurrent.

The experimental method to detect the photoinitiated processes in the femtosecond time scale is pump-probe transient absorption spectroscopy (TAS). This technique uses ultrashort laser pulses to trigger and trace photophysical and photochemical processes. Two laser pulses are used; a pump pulse to excite the sample and start the dynamics followed by a probe pulse to obtain the absorption spectrum of the excited sample. A delay is introduced between the arrival time at the sample of the pump and the probe pulses. The absorption spectra are then recorded for each delay time. The change in time of the absorption spectra indicates the change in population of molecular states, hence the charge dynamics within the sample.

To cover all the photoinitiated dynamics occurring within a photovoltaic cell at the same time using pump-probe transient absorption spectroscopy, the probe pulse had to be of a broad spectral range. The development of a source of a femtosecond probe laser pulse covering a broad spectral region was one of the main objectives of this project.

The commercially available femtosecond lasers are centred around one wavelength value and the conversion of their spectral contents requires an external wavelength conversion technique. A noncollinear optical parametric amplifier (NOPA) [11] is such a wavelength converting tool. In this optical setup a beam of high intensity (the pump) amplifies a beam of lower intensity (the signal) and at the same time another beam is generated (the idler). In our setup the source of the signal and pump pulses is a regenerative Ti:Sa amplifier system (Clark MXR CPA 2101) producing pulses of central wavelength of 775 nm. The signal to be amplified is a white light continuum pulse ($470 - 700$ nm) generated by focusing the 775 nm laser beam onto a Yttrium aluminium garnet (YAG) or a Sapphire crystal. The pump is the second harmonic of the fundamental pulse centred at 387nm. The parametric amplification process takes place in a beta barium borate (BBO) crystal where both the pump and the signal to be amplified are spatially and temporally overlapped. In this work the range of the pulses produced by the NOPA has been extended up to 2500 nm by utilizing the idler pulse instead of the amplified signal. The idler pulse provides a spectral window in the near infrared range 900-2500 nm to probe the charge dynamics within the indoline D216/electrodeposited ZnO dye sensitized solar cells as well as the dynamics in the fluorinated zinc phthalocyanine F_nZnPc/C_{60} ($n = 0, 4, 8, 16$) organic solar cells.

The temporal resolution of a transient absorption measurement is defined by the duration of both the pump and the probe pulses. Therefore, the temporal characterization of the produced near infrared probe pulse was necessary. The phase and amplitude of the generated pulse was retrieved using cross correlation frequency resolved optical gating (XFROG) [12]. The conventional autocorrelation pulse characterization technique only gives an estimate of the duration of the envelope of the pulse whereas the XFROG resolve the spectral components of the pulse and provides information about the phase of the pulse.

The following chapter introduces the pump-probe transient absorption experimental setup and the newly developed source of near infrared pulses. Chapter three presents the results obtained by using the generated pulses in the investigation of charge transfer processes within indoline D216/electrodeposited ZnO dye sensitized solar cells and fluorinated zinc phthalocyanine F_nZnPc/C_{60} ($n = 0, 4, 8, 16$) organic solar cells. Chapter four explains the experimental procedure followed in the characterization of the generated pulses.

2. Transient Absorption Spectroscopy In the Near Infrared Spectral Domain

In this chapter, the experimental procedure followed to obtain a transient absorption (TA) spectrum that has a probe window in the near infrared range is presented. As mentioned in Chapter 1 the production of such a spectrum requires two ultrashort laser pulses namely the pump and the probe. The pump pulse initiates the charge dynamics within the sample under study by photoexciting its molecules. The absorption spectrum of these molecules is then detected by the probe pulse. The absorption spectrum of a molecular system is directly linked to the charge population of its molecular states. Therefore, the charge dynamics within the sample are concluded from the change in absorption spectra, that are recorded when sending the probe pulse at delayed times with respect to the pump pulse. The simultaneous detection of various charge dynamics requires a probe pulse that can cover a broad spectral range.

The laser in our laboratory is a regenerative Ti:Sa amplifier system (Clark MXR CPA 2101) that consists of a femtosecond fibre laser, a stretcher, a Ti:Sa regenerative amplifier and a compressor. It delivers pulses with a duration of 150 fs, 775 nm central wavelength and 800 μJ energy per pulse at a repetition rate of 1 KHz. The spectral contents of the pulse out of this amplifier system had to be tuned to produce a probe pulse that covers a broad spectral range. The wavelength conversion techniques used in our laboratory to tune the central wavelength of the output pulse is discussed in this chapter. A typical TA spectrum produced by our experimental setup as well as the method followed to analyse and extract information from it is also presented.

2.1 Characteristics and Propagation of Femtosecond Laser Pulses

A femtosecond laser pulse is an electromagnetic wave packet[13] of a defined temporal profile shape and a duration in the scale 10^{-13} - 10^{-14} s. The temporal profile of the pulse is known as its envelope. The duration Δt of a pulse that has a Gaussian shaped envelope can be defined as the full width at half maximum (FWHM) of that envelope. The mathematical representation that will be used in this work to describe the electric field component of a femtosecond pulse is:

$$E(t) = Re[E_0\, e^{\frac{-t^2}{\tau^2}}\, e^{-i\omega_0 t+\phi(t)}]; \tag{2.1}$$

where E_0 is the amplitude of the electric field, τ is temporal profile width at $1/e$ of the maximum electric field, ω_0 is its carrier frequency and $\phi(t)$ is its time dependent phase. The width τ was used in this representation instead of the duration Δt to simplify further calculations. The relation between the two parameters is $\tau = \frac{\Delta t}{2\sqrt{\ln 2}}$.

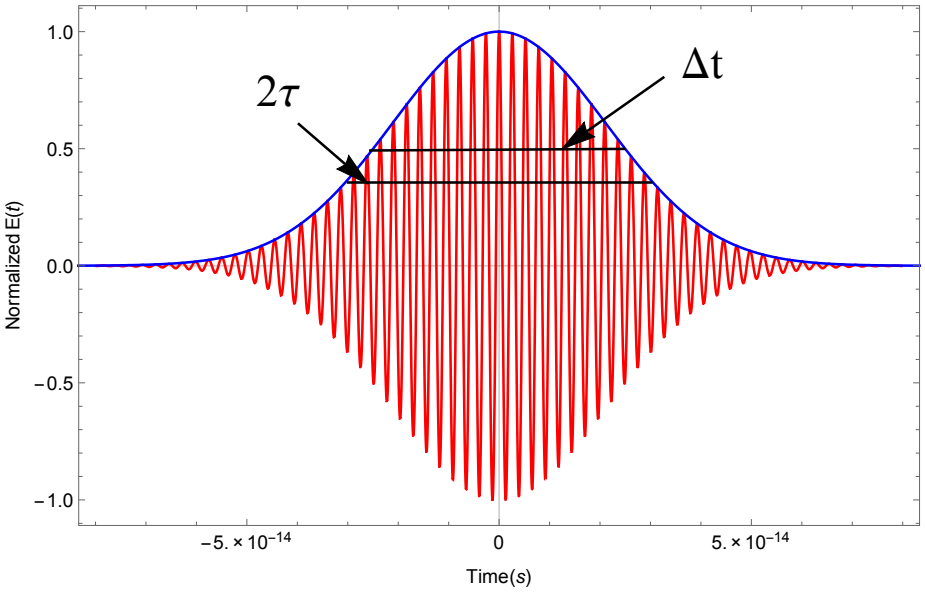

Figure 2.1: Temporal evolution of the electric field (red line) and envelope (blue line) of a pulse of 775 nm central wavelength and 50 fs FWHM. The temporal width 2τ for this pulse is 60 fs.

Figure 2.1 shows the electric field of a pulse that has a duration of 50 fs and a constant phase. All spectral components of such a pulse propagate with the same speed and it is known as a Fourier transform limited pulse. The duration Δt and spectral width $\Delta\omega$ of this pulse minimize the bandwidth-duration product defined by [14]:

$$\Delta t \times \Delta\omega \geq 2\pi \times 0.441. \tag{2.2}$$

In frequency domain the electric field of such a pulse is the Fourier transform of its time dependent electric field:

$$E(\omega) = \int_{-\infty}^{\infty} E(t)e^{i\omega t}dt \propto \int_{-\infty}^{\infty} e^{\frac{-t^2}{\tau^2}} e^{i(\omega-\omega_0)t}dt = \tau\sqrt{\pi}e^{\frac{-(\omega-\omega_0)^2}{4/\tau^2}}. \tag{2.3}$$

The pulse has a Gaussian-shaped spectral profile with a $1/e$ spectral width $\omega = \frac{\Delta\omega}{2\sqrt{\ln 2}} = 2/\tau$.

When a Fourier transform limited pulse propagates through a dielectric medium, its spectral components differ in propagation speed due to dispersion (see Appendix 5 for details). Therefore, the electric field of this pulse will oscillate with a time varying frequency $\omega(t)$. The pulse beyond the dielectric medium is then referred to as a chirped pulse. The phase of a chirped pulse is related to its instantaneous frequency $\omega(t)$ by [13]:

$$\omega(t) = \omega_0 + \frac{d}{dt}\phi(t). \tag{2.4}$$

Assuming a linear chirp (i.e. a linear dependence of the frequency on time), that is a quadratic phase $\phi(t) = Ct^2$, the electric field of the chirped pulse will be:

$$E(t) = Re[E_0\, e^{\frac{-t^2}{\tau^2}}\, e^{-i(\omega_0+Ct)t}]; \tag{2.5}$$

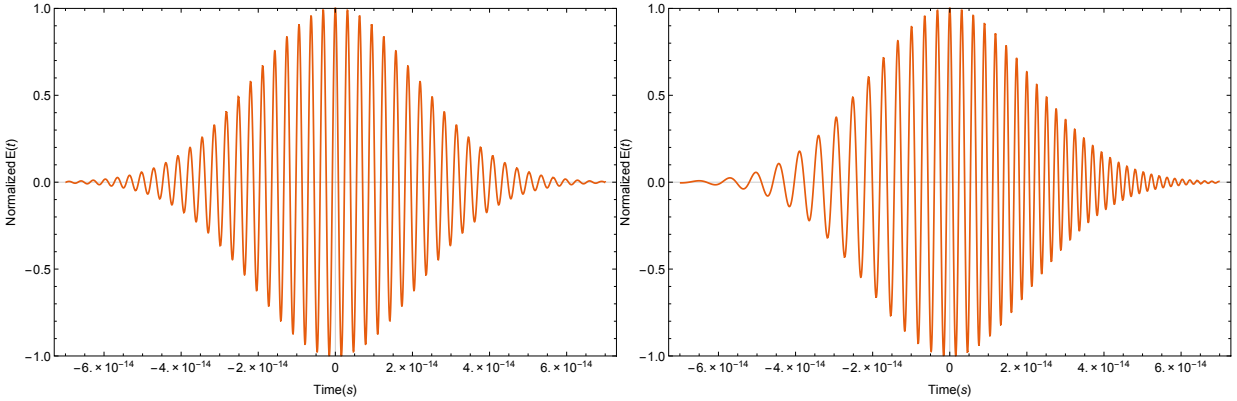

(a) Unchirped **(b)** Chirped

Figure 2.2: Illustration of the temporal evolution of the electric field of (a) a Fourier transform limited pulse (unchirped pulse) and (b) a pulse of a time-dependent phase (chirped pulse). The duration of both pulses is 50 fs and their central wavelength is 1 μm. A quadratic positive chirp($C = (10^{14})^2 \mathrm{s}^{-2}$) was assumed in the simulation of the chirped pulse.

where C is a constant that has units of s^{-2}.

The electric field oscillations of a Fourier transform limited pulse and those of a positively chirped pulse are illustrated in Figure 2.2. The two pulses have the same amplitude and duration $\Delta t = 50$ fs. The frequency of the chirped pulse increases with time while it remains unchanged for the transform limited pulse. As shown in the figure, the low frequency components (red components) are at the front of the positively chirped pulse whereas the high frequency components (blue components) are at the back.

The electric field of the chirped pulse in frequency domain is the Fourier transform of the expression (2.5):

$$\begin{aligned} E(\omega) = E_0 \int_{-\infty}^{\infty} E(t) e^{i\omega t} dt &= E_0 \int_{-\infty}^{\infty} e^{-t^2/\tau^2} e^{-i(\omega_0 t + Ct^2)} e^{i\omega t} dt \\ &= E_0 \int_{-\infty}^{\infty} e^{-(\frac{1}{\tau^2} + iC)t^2} e^{i(\omega - \omega_0)t} dt. \end{aligned} \tag{2.6}$$

Using $\int_{-\infty}^{\infty} e^{-at^2} e^{ibt} = \frac{\sqrt{\pi}}{\sqrt{a}} e^{-\frac{b^2}{4a}}$ and separating the real and imaginary parts, the integration (2.6) can be solved to give the amplitude and phase of the electric field of the chirped pulse in frequency:

$$\begin{aligned} E(\omega) &= E_0 \ \frac{\sqrt{\pi}}{\sqrt{\frac{1}{\tau^2} + iC}} \quad e^{-\frac{(\omega-\omega_0)^2}{4(\frac{1}{\tau^2} + iC)}} \\ &= E_0 \ \frac{\sqrt{\pi}}{(\frac{1}{\tau^4} + C^2)^{1/4}} \quad e^{-\frac{(\omega-\omega_0)^2}{\frac{4}{\tau^2}(1 + C^2\tau^4)}} \quad e^{i\left[\frac{(\omega-\omega_0)^2}{\frac{4}{\tau^2}(\frac{1}{C\tau^2} + C\tau^2)} - \frac{1}{2}\tan^{-1}(C\tau^2)\right]} \\ &= E_0 \ \left[\frac{\sqrt{\pi}}{(\frac{1}{\tau^4} + C^2)^{1/4}} \quad e^{-\frac{(\omega-\omega_0)^2}{\frac{4}{\tau^2}(1 + C^2\tau^4)}}\right] \quad \left\{e^{i\left[\alpha(\omega-\omega_0)^2 - \beta\right]}\right\}; \end{aligned} \tag{2.7}$$

where $\alpha = \frac{C\tau^4}{4(1+C^2\tau^4)}$ and $\beta = \frac{1}{2}\tan^{-1}(C\tau^2)$ are constants. The term in brackets in the above expression represents the spectral amplitude of the chirped pulse. The term shows that the pulse maintains its Gaussian-shaped envelope after propagating through the dispersive medium. Its spectral width however, will be broader by a factor of $\frac{C\tau^2}{(1+C^2\tau^4)}$ than the unchirped pulse represented by Equation (2.3). Bearing in mind that in this calculation the duration of the pulse was kept constant, an increase in the spectral width will increase the bandwidth duration product of Equation 2.2. This proves that the product is a minimum only for a transform limited pulse. One can also conclude an increase in this product by introducing the chirp in the frequency domain keeping the spectral width unchanged. In that case the increase in the product is attributed to an increase in the duration of the pulse. The second exponent in braces indicates that the chirped pulse will have a phase of a quadratic dependence on frequency.

The pulse out of our amplifier system has a Gaussian-shaped envelope of 150 fs duration. At optimum compression this pulse is assumed to be Fourier transform limited. However, as it propagates through various optical elements on the setup both its spectral contents and duration change. These changes are not only caused by the normal dispersion as discussed above, but also by nonlinear properties of the media that the pulse passes through. These properties are stimulated by the high intensity of the pulse (average of $\sim 10^{13}$ W/cm^2).

The dependence of the optical properties of a medium on the strength of the electric field of an incident pulse can be represented by expanding the polarization of the medium in terms of the electric field of that pulse [13]:

$$P(E) = \epsilon_0\chi(E)E = \epsilon_0\chi^{(1)}E + \epsilon_0\chi^{(2)}E^2 + \epsilon_0\chi^{(3)}E^3 + ... \tag{2.8}$$

where $\chi(E)$ is the optical susceptibility. All linear responses of the medium such as absorption and reflection are described by the first term in the above expansion. Higher terms in the expansion represent the responses that depend in a nonlinear manner on the strength of the electric field. A variety of nonlinear processes are described by these terms, of interest to this work are: second harmonic generation, white light generation and second harmonic generation.

2.2 Frequency Conversion Techniques

Second Harmonic Generation (SHG)

The central frequency of a femtosecond pulse is shifted to double its value after it propagates through a crystal which has a non zero second order susceptibility[14]. The process by which the frequency of the pulse is doubled is known as second harmonic generation (SHG). It can be described using the second term in the polarization expansion (2.8):

$$P^{(2)}(E) = \epsilon_0\chi^{(2)}E^2(t) = \epsilon_0\chi^{(2)}|E_0|^2\, e^{\frac{-2t^2}{\tau^2}} e^{-i(2\omega_0)t}. \tag{2.9}$$

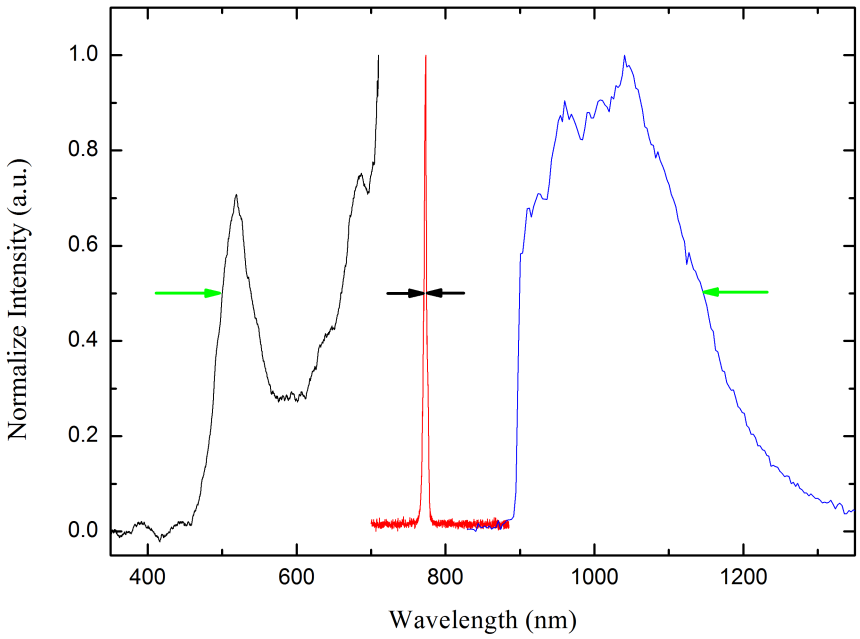

Figure 2.3: White light continuum generated by using the pulse out of the amplifier system centered around 775 nm (red) to pump a Yttrium aluminium garnet (YAG) crystal. The continuum extend from 450 nm in the visible (black) to 1400 nm in the near infrared.

The expression above explains that a source of a new electromagnetic wave oscillating with double the frequency of the incident laser pulse ($2\omega_0$) will be generated.

In the quantum picture, second harmonic generation can be described as the annihilation of two photons of frequency ω_0 and the simultaneous creation of one photon of frequency $2\omega_0$. Energy and momentum are conserved in this process therefore;

$$\hbar\omega_0 + \hbar\omega_0 = 2\hbar\omega_0; \tag{2.10}$$

and

$$\Delta\vec{k} = \vec{k}(2\omega_0) - \vec{k}(\omega_0) - \vec{k}(\omega_0) = 0. \tag{2.11}$$

The momentum conservation relation 2.11 is also known as the phase matching condition. The phase matching condition is fulfilled by adjusting the crystal orientation with respect to the incident beam. Under a different phase matching condition the inverse of second harmonic generation is also possible; one photon of frequency ω can be annihilated to create two photons of half its frequency.

White Light Continuum Generation (WLG)

A beam of femtosecond laser pulses that is focused onto a nonlinear crystal such as a Yttrium aluminium garnet (YAG), a Sapphire or a Calcium Fluoride (CaF_2) crystal, experiences severe broadening of spectrum causing it to appear as a white light spot

surrounded by rings when projected on a paper.

This spectral broadening effect is known as white light generation (WLG) [15] and is often attributed to the intensity dependent refractive index of the medium that the pulse propagates through, that is the Kerr nonlinearity of the medium. Figure 2.3 shows the white light continuum generated by pumping a 3 mm YAG crystal by the 775 nm pulse out of our amplifier system. This continuum extends from 470 nm in the visible to 1400 nm in the near infrared.

The refractive index n dependence on the average intensity I is given by[16]:

$$n = n_0 + n_2 I; \tag{2.12}$$

where n_0 is the linear refractive index of the Kerr medium and n_2 is the refractive index describing the change introduced by the nonlinearity of the medium. This nonlinear refractive index is given by:

$$n_2 = \frac{3}{2n_0^2 \epsilon_0 c} \chi^{(3)}; \tag{2.13}$$

where ϵ_0 is the permittivity of free space, c is the speed of light and χ_3 is the third order susceptibility [16]. Due to the symmetry of the WLG crystals the second order susceptibility, and so the second term in the expansion (2.8), is zero and has no contribution to this nonlinear process. The white light generation is a third order nonlinear process.

A beam of a Gaussian spatial intensity distribution passing through a nonlinear crystal with a positive n_2 will experience higher values of the refractive index n at its center, where the intensity is maximum, than at the wings[16]. This causes the central components of the beam to travel slower than the components at the wings forcing the beam to come to a focus within the crystal. This effect is known as self focusing as the high intensity of the beam stimulates the crystal to act as a focusing lens. The beam is focused tighter and tighter as it propagates through the crystal due to the increasing intensity. However, such a beam will not collapse into a focal point because self focusing will be stopped by diffraction as the beam size approaches the diffraction limit of the crystal.

A femtosecond laser pulse can be viewed as a stack of infinitely thin slices of transverse waves under the assumption of a dispersionless medium and a slowly varying envelope approximation [17]. Like a Gaussian beam, each slice will self focus to a point of maximum intensity depending on its power. Therefore, the slice at the center of the pulse will create a spike of maximum intensity. Self focusing contributes to the process of white light generation [18] but does not provide a full description of such a severe broadening of the spectrum of the incident beam.

The main process to which white light generation is attributed is self phase modulation (SPM). This process is explained by considering the time dependent intensity of the pulse $I(t) \propto |E|^2 = e^{-\frac{2t^2}{\tau^2}}$. Assuming that the pulse has propagated a fixed distance x

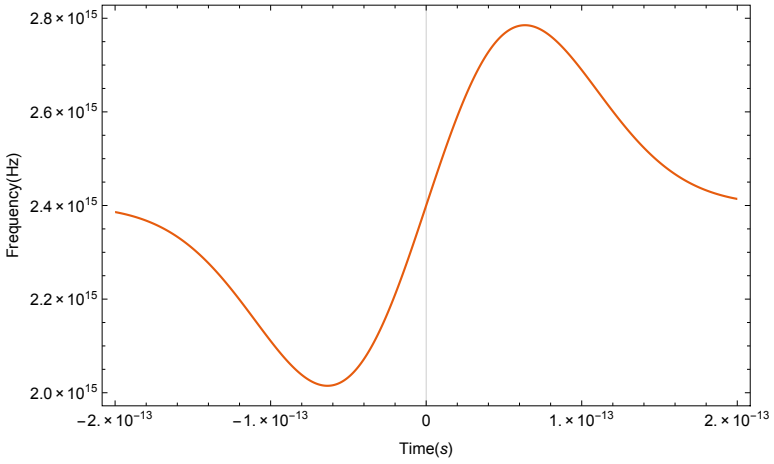

Figure 2.4: The instantanous frequency of a self phase modulated pulse of a central frequency 2.4×10^{15}Hz.

through the medium, its time dependent phase will be:

$$\phi(t) = \frac{\omega_0 n(t) x}{c} - \omega_0 t = \omega_0 n_0 \frac{x}{c} + \omega_0 n_2 I(t) \frac{x}{c} - \omega_0 t. \tag{2.14}$$

The instantaneous frequency will therefore be:

$$\omega(t) = -\frac{d\phi(t)}{dt} = \omega_0 - \frac{4}{\tau^2}\, n_2 \omega_0\, \frac{x}{c}\, t e^{\frac{-2t^2}{\tau^2}}. \tag{2.15}$$

Figure 2.4 shows the frequency of a phase modulated pulse centered at 775 nm. Self phase modulation result in the generation of new spectral components of low frequencies (red shifted) at the leading edge of the pulse and new high frequencies (blue shifted)at the back of the pulse. Moreover, the pulse will now be chirped (although the medium was assumed to be dispersionless) as different spectral components within the pulse have different propagation times.

Optical Parametric Amplification (OPA)

When a beam of femtosecond pulses with centeral wavelength of 387 nm is overlapped spatially with a white light continuum beam in a BBO crystal a reduction in the intensity of the beam, a production of an intense visible beam (470 - 700 nm) and a creation of a near infrared beam (850 - 2400 nm) is observed. These new beams emerge from the BBO as a result of optical parametric amplification, a second order nonlinear response of the crystal to the intense incoming beams. The second term of the polarization expansion 2.8 will be in this case:

$$P^{(2)}(E) = \epsilon_0 \chi^{(2)} E_p E_s^* = \epsilon_0 \chi^{(2)} e^{-t^2(\frac{1}{\tau_p^2}+\frac{1}{\tau_s^2})} e^{-i(\omega_p - \omega_s)t}; \tag{2.16}$$

where the subscripts p and s refer to the second harmonic pump and the visible signal respectively. The polarization term 2.16 predicts the creation of a new electromagnetic wave of central frequency$(\omega_p - \omega_s)$.

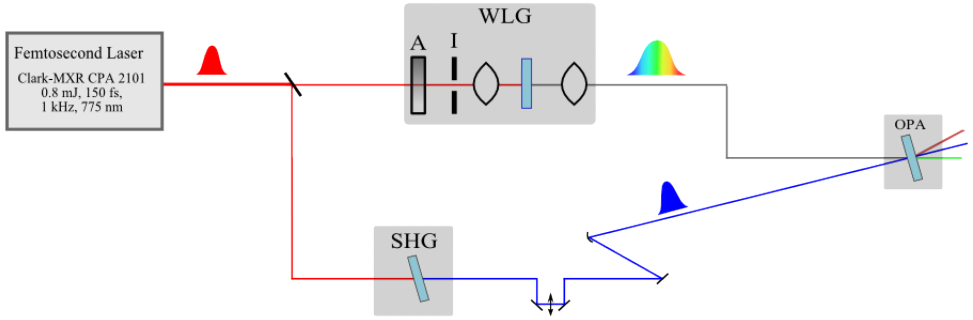

Figure 2.5: Schematic of the Non collinear Optical Parametric Amplifier. A: Attenuator, I: Iris, WLG: White Light Generation, SHG: Second Harmonic Generation, OPA: Optical Parametric Amplification.

Optical parametric amplification (OPA) is described in the photon picture as the creation of two photons as a result of the annihilation of a pump photon. The splitting of the pump photon is stimulated by a seeding photon. Therefore, one of the two photons created will be forced to have the same energy as the seeding photon while the other will have what remains from the pump's energy. The pump, the seeded photon and the energy leftover photon (the idler) have the following energy relation:

$$\hbar\omega_p = \hbar\omega_s + \hbar\omega_i. \tag{2.17}$$

The phase matching condition for this process is:

$$\Delta\vec{k} = \vec{k}(\omega_p) - \vec{k}(\omega_s) - \vec{k}(\omega_i) = 0. \tag{2.18}$$

Figure 2.5 is a schematic of the commercially available noncolinear optical parametric amplifier(NOPA), an optical setup that is conventionally used to amplify beams of low intensities. The beam out of the laser is split within the NOPA into two beams using a 50% beam splitter. One beam to generate white light continuum and the other beam to generate the second harmonic. The white light is generated by focusing the incoming beam into either a YAG or a sapphire crystal. A linear attenuator and an iris were used to control the intensity and spatial distribution of the incoming beam. The white light continuum beam is focused in front of the second BBO crystal using a lens. The second harmonic is also focused in front of the BBO using a spherical mirror. The two beams are overlapped spatially in the BBO crystal.

The white light continuum provides the seeding signal that stimulates the splitting of the energy of the pump photons. This continuum is chirped, therefore each of its temporal components overlap with the pump at a different time. The component selected to overlap with the pump is referred to as the signal and will be amplified within the second BBO crystal. The selection of a specific component depends on the arrival time of the pump pulse to the second BBO. A mirror mounted on a translation stage is introduced in the path of the pump pulse, as can be seen in Figure 2.5, to control its arrival time. In the optical parametric amplification process, taking place within the second BBO crystal, the value of the pump pulse's wavelength was kept a constant allowing for the idler wavelength to change according to the wavelength of the seeding signal. Therefore, various pulses of wavelengths in the visible and near

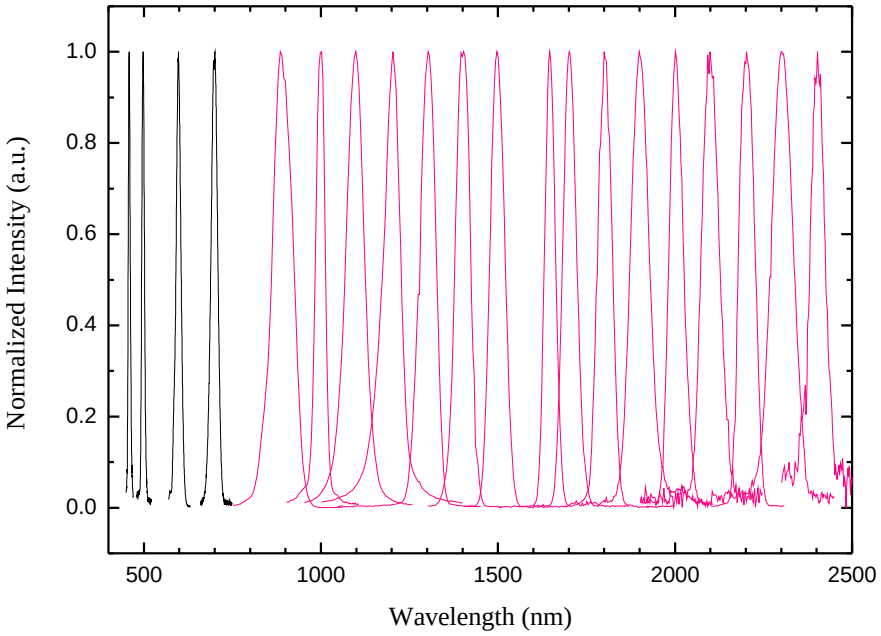

Figure 2.6: Spectra of the pulse produced by the NOPA. The visible pulses up to 700 nm (black) are produced using the signal of the NOPA whereas the pulses 900 - 2400 nm (pink) are produced using the idler.

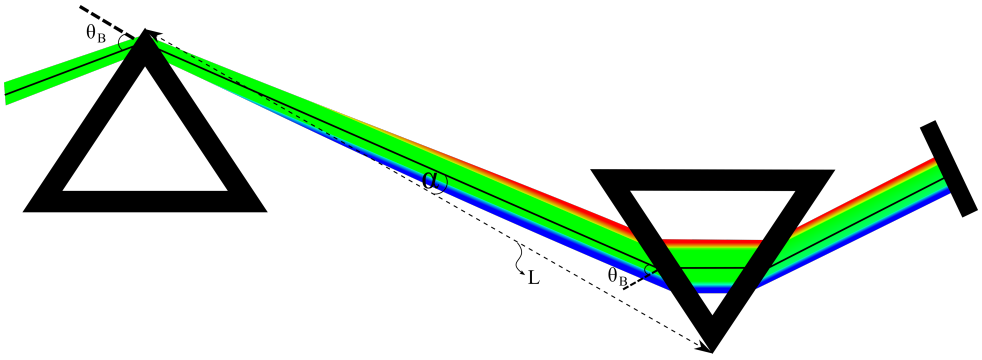

Figure 2.7: A two prisms compressor

infrared ranges are produced by the NOPA when either choosing the signal or the idler as a source. Figure 2.6 shows the spectra of the pulses produced by the NOPA in the visible and near infrared ranges.

2.3 Pulse Compression

One way to compensate for the chirp of a femtosecond pulse caused by its propagation through optical transparent media is by using a two prism compressor. A pair of prisms is used to create a negative dispersion such that the spectral components at the leading edge of the chirped pulse travel a longer distance than the components at the

back[19][20]. Figure 2.7 portrays the two-prism compressor that is used in our laboratory to create an optical path that results in a negative dispersion of the pulse. The two prisms are identical, having the same apex angle and coating. They are aligned such that the surface at which the beam enters the first prism (entrance surface) is parallel to the surface at which the beam exits the second prism (exit surface). The prisms are cut so that the angle of minimum reflection is the Brewster angle.

Depending on the central wavelength of the beam, the angle of incidence is set to Brewster angle by rotating the tip of the first prism. The different spectral components of the temporally dispersed beam then diffuse along the second prism travelling different distances depending on the angle of dispersion. The second prism is mounted on a translation stage perpendicular to its base to change the distance each of the components travel within the prism. As can be seen in Figure 2.7 the red components (short frequency components) will be forced to travel a longer distance within the second prism than the blue components (long frequency components) due to the geometry of the setup. The tip of the second prism is then rotated so that the angle of incidence is set to the Brewster angle ensuring that the two prisms are parallel. Finally, a folding mirror is placed behind the second prism to send the beam back through the two prisms with a slight vertical change in position in order to separate the incoming and outgoing beams. The spatial dispersion made by the first prism is then corrected by the first prism as the beam exits the compressor.

The phase delay introduced by such a compressor depends on the total optical path that the beam travels through the compressor. This optical path is given by [19]:

$$P = 2L\cos\alpha; \tag{2.19}$$

where L is the distance from the tip of the first prism to the tip of the second prism and α is the angle between a beam travelling from the inner surface of the first prism to the bulk of the second prism and a reference beam that travels tip to tip. The path beyond the second prism does not contribute to the negative dispersion because the beam is then collimated and all of its components travel the same distance hence this path was not included in the expression above. The amount of dispersion introduced by the two prism compressor is calculated from the second derivative of the path P in Equation (2.19) [19] such that:

$$\frac{d^2P}{d\lambda^2} = 4L\left[\left(\frac{d^2n}{d\lambda^2} + (2n - \frac{1}{n^3})(\frac{dn}{d\lambda})^2\right)\sin\alpha - \left(2(\frac{dn}{d\lambda})^2\right)\cos\alpha\right]; \tag{2.20}$$

where n is the index of refraction of the prism. Approximating $cos\alpha$ to unity and estimating $L\sin\alpha$ to be twice the diameter of the beam D [19], equation (2.20) can be simplified to:

$$\frac{d^2P}{d\lambda^2} = 4\left[\frac{d^2n}{d\lambda^2} + (2n - \frac{1}{n^3})(\frac{dn}{d\lambda})^2\right]2D - 4L\left[2(\frac{dn}{d\lambda})^2\right]. \tag{2.21}$$

The first term in the dispersion expression above depends on the path of the beam within the prisms, whereas the second term depends on the separation between the

two prisms. Therefore, by adjusting the separation between prisms and the distance that the beam travels within the second prism, the amount of negative dispersion that the compressor introduces to the chirped pulse can be controlled and maximum compression can be achieved.

As an illustrative example the material parameters listed in Reference [21] can be used to calculate the phase delay caused by the two prisms compressor in our setup on a beam of a central wavelength of 550 nm. These parameters are obtained using Sellmeier's equations. For our fused silica prisms these parameters are $n = 1.46$, $\frac{dn}{d\lambda} = -0.04218$ μm^{-1} and $\frac{d^2n}{d\lambda^2} = 0.2135$ μm^{-2}. Substituting these parameters into Equation (2.21), the negative dispersion in terms of the prisms separation is:

$$\frac{d^2P}{d\lambda^2} = 1.744\ \mu m^{-1} - (0.014 \times 10^{-3}\ \mu m^{-2})\ L. \tag{2.22}$$

2.4 Transient Absorption Spectrum

As mentioned in Chapter 1 the motive behind the development of a near infrared pulse source was to use that source in the investigation of femtoseond photoinduced charge dynamics within solar cells. Pump probe transient absorption spectroscopy (TAS) is the experimental technique by which the change in spectra of photoexcited molecules at different times after photoexcitation can be monitored. The changes in the spectra indicate changes in the molecular states population. Therefore, tracing these spectral changes in time allowed to detect the charge dynamics within these molecules. Two femtosecond pulses are required to produce a transient absorption spectrum: a pump pulse to excite the molecules of the sample and a probe pulse to obtain the absorption spectrum of the excited molecules.

Experimental Setup

Figure 2.8 is a schematic of the pump probe transient absorption spectroscopy setup in our laboratory. To generate the pump and probe pulses, the beam out of the amplifier system is split into two paths (Path 1 and Path 2 in the figure). Along path 1 the pump pulse is generated using a non collinear optical parametric amplifier (NOPA 1). The central wavelength of the input pulse is tuned in NOPA 1 to the maximum absorption wavelength of the sample under study. This value is determined from the sample's steady state absorption spectrum. The pump pulse wavelength can be tuned between 470 nm to 700 nm and has a sub 100 fs duration. The pulse out of the NOPA is sent to the two-prism compressor to reduce its duration to the minimum value allowed by its spectral components. The compressor reduces the duration of the pulse to sub 50 fs.

The probe pulse is generated along Path 2. It is produced by either a 3 mm YAG crystal using the laser pulse out of the amplifier system as a pump, or from the idler of NOPA 2. The spectral range of the white light continuum generated by the YAG crystal in the near infrared is 900 - 1400 nm. Such a broad spectral range allows for simultaneous detection of various spectral signatures of transient species. The duration

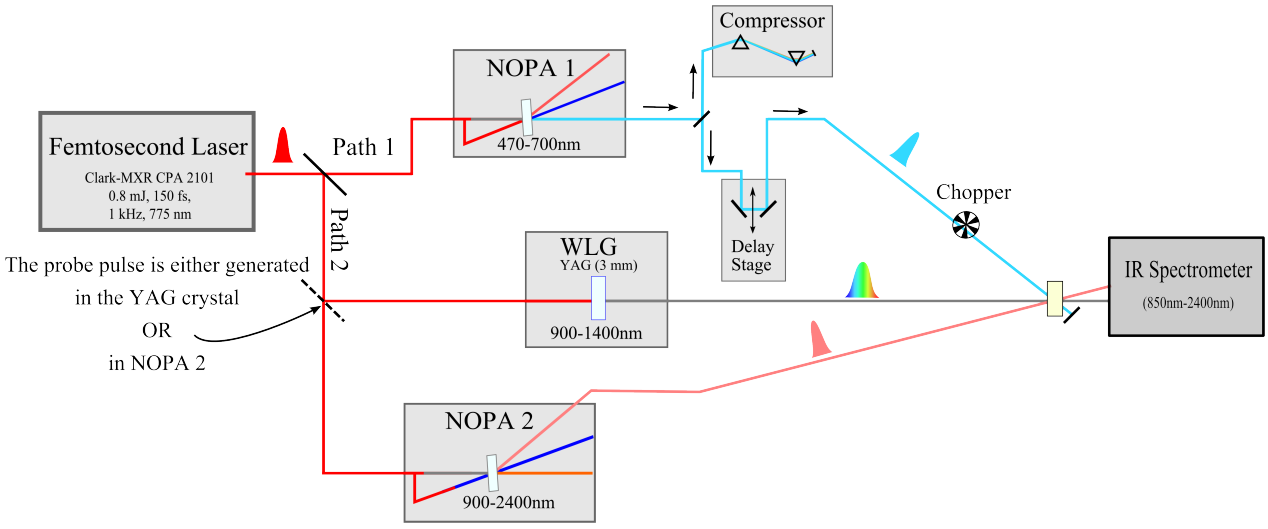

Figure 2.8: A schematic of the pump probe transient absorption spectroscopy experimental setup.

of the white light pulse is $>$ 150 fs. Since the resolution of a pump probe transient absorption measurement is defined by the convolution of the pump and the probe pulses, the resolution of a NOPA pump - white light probe measurement is sub 200 fs. The probe pulse generated using the idler of NOPA 2 has a centeral wavelength tunable between 900 to 2400 nm. The temporal resolution of a NOPA pump NOPA probe measurement was observed from the transient absorption measurements to be $\sim$ 150 fs (see Chapter 3 for details).

The pump pulse out of the compressor is sent to the sample through two folding mirrors mounted on a 10 cm long computer-controlled mechanical translation stage. The optical path of the pump pulse can therefore be adjusted by moving the delay stage. The stage allows a minimum step size of 2 μm which corresponds to a 13 fs delay.

Experimental Method

Along Path 2 the probe pulse is generated either as a continuum in the YAG crystal or as a narrow band beam in NOPA 2. The probe beam is sent, directly after generation, to the sample. Along Path 1 the pump pulse is generated by tuning the central wavelength of the laser output to the maximum absorption wavelength of the sample using the noncollinear optical parametric amplifier (NOPA 1). The signal beam out of NOPA 1 is then directed to the two prism compressor to shorten the duration of the pump pulse to sub 50 fs. The pulse is then sent to the sample through a mechanical delay stage to control its arrival time. The translation stage is set to move in time steps of 50 fs, 100 fs and 1 ps to create a short, an intermediate and a long time scan windows. A chopper is placed behind the delay stage to block every second pulse of the pump beam. This way a reference unpumped spectrum is recorded by the spectrometer after the pumped spectrum. The change in optical density is then calculated using;

$$\Delta OD(\lambda) = -\log \frac{I(\lambda)}{I_0(\lambda)}; \tag{2.23}$$

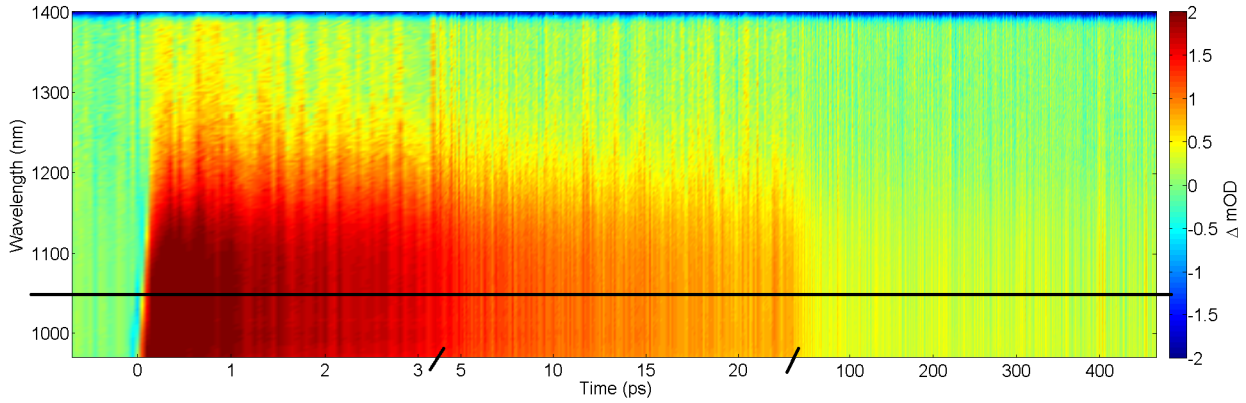

Figure 2.9: Transient absorption spectrum of C_{60} in the short (50 fs), intermediate (100 fs) and long scan (1 ps) window with a 480 nm pump and a white light continuum probe. A horizontal lineout is taken from spectrum at 1050 nm.

where I and I_0 are the intensities of the pumped and the unpumped transmission spectra of the sample. The recorded spectra are averaged over 6000 shots.

A Typical Visible-pump near-infrared-probe transient absorption spectrum

NOPA pump white light probe measurement

Figure 2.9 shows the transient absorption spectrum of a C_{60} film on a glass substrate at 50 fs, 100 fs and 1 ps time steps. The x axis shows the delay time between the pump and probe pulses, the y axis shows the wavelength and the change in optical density is shown as a color code. A negative change in the optical density indicates a reduction of the absorption and is shown in blue in the color map. A reduction in the absorption spectrum could be due to groud state bleach (GSB) or to stimulated fluorescence. A positive change in optical density indicates more light absorption and is shown in red. This signal is due to excited state absorption (ESA).

The pump pulse's central wavelength was set in this measurement to 480 nm, a value determined from the steady state absorption spectrum of C_{60}. The probe pulse was a white light continuum produced in a YAG crystal and extending from 900 nm to 1400 nm. This spectral window was chosen to detect self ionization of C_{60}, a process by which a molecule of C_{60} interacts with another neighbouring molecule to produce a C_{60}^{-} anion. The absorption of the C_{60}^{-} anion is known to be at 1050 nm [22]. A horizontal lineout at 1050 nm was extracted from the transient absorption spectrum of the C_{60} thin film to determine the decay time of the absorption signal. As can be seen in Figure 2.10 the trace obtained was fitted using the biexponential decay function:

$$f(t) = A_0 + A_1 e^{\frac{-x}{t_1}} + A_2 e^{\frac{-x}{t_2}}; \tag{2.24}$$

where $A_0 = 0.26$ is the amplitude of the baseline, $A_2 = 0.37$ and $A_2 = 0.37$ are the amplitudes associated with the two time constants t_1 and t_2, respectively. This absorption signal was found to decay with a short time constant $t_1 = 3$ ps and a long

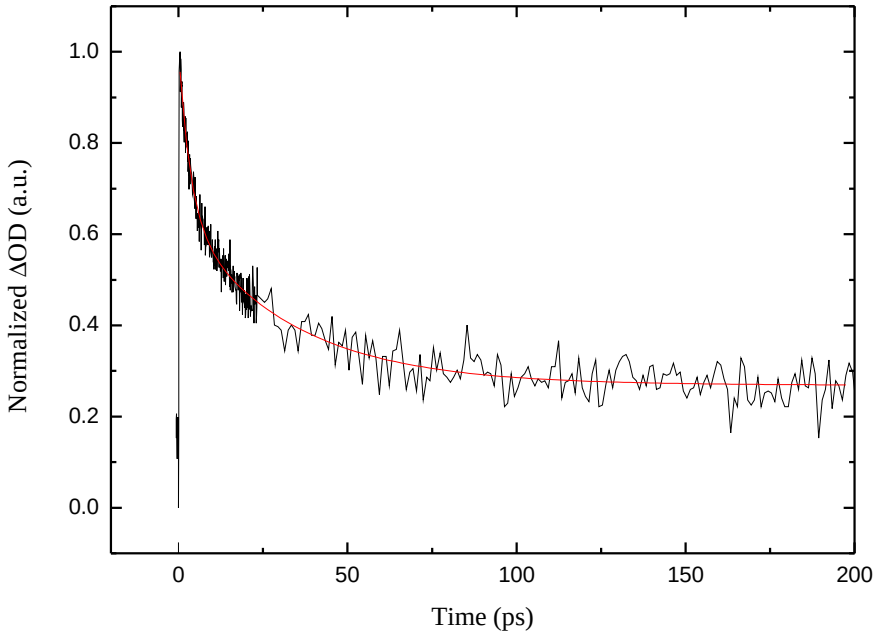

Figure 2.10: Temporal trace of the excited state absorption of C_{60} extracted at 1050 nm from the transient absorption spectrum of a C_{60} thin film with a 480 nm pump and a white light contiuum probe. The trace was fitted with a biexponential decay function and two constant were found to be $t_1 = 3$ ps and $t_2 = 32$ ps.

time constant $t_2 = 32$ ps. The assignment of these two time scales and more details about this measurement will be presented in Chapter 3.

NOPA pump NOPA probe measurement

Figure 2.11 is the transient absorption spectrum of the dye sensitized solar cell made by sensitizing nanoporous ZnO with the indoline dye DN216 [1]. The dye is the light absorber in this cell and the ZnO is the electron acceptor. The central wavelength of the pump was set to the maximum absorption of the dye at 530 nm. The probe pulse is the narrow band ($\Delta\lambda \sim 11$ nm) NOPA idler pulse centred at 2160 nm. This probe window allows for the detection of the change in the population of the conduction band of ZnO. Upon photoexcitation electrons are believed to be injected into the conduction band of ZnO.

A horizontal lineout was taken from the transient spectrum at 2160 nm to detect the temporal trace of the electrons in the conduction band of ZnO. The long time window is shown in Figure 2.12. This signal was found to rise with three time constant $t_1 = 200$ fs, $t_2 = 2$ ps and $t_3 = 10$ ps. The three time constants were interpreted as the direct injection of electrons from the excited state of the dye to the conduction band of the ZnO ($t_1 = 200$ fs) and injection via intermediate states ($t_2 = 2$ ps and $t_3 = 10$ ps) [1]. Details of this measurements and analysis will be presented in Chapter 3

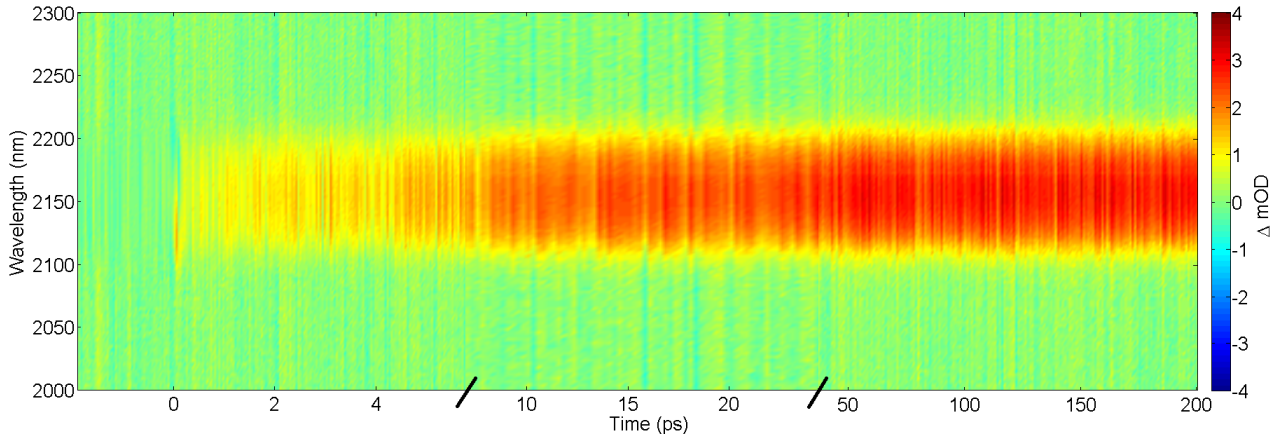

Figure 2.11: Transeinet absorption spectrum of the indoline dye DN216/ZnO dye sensitised solar cell with pump pulse central wavelength of 530 nm and NOPA probe pulse centered around 2160 nm.

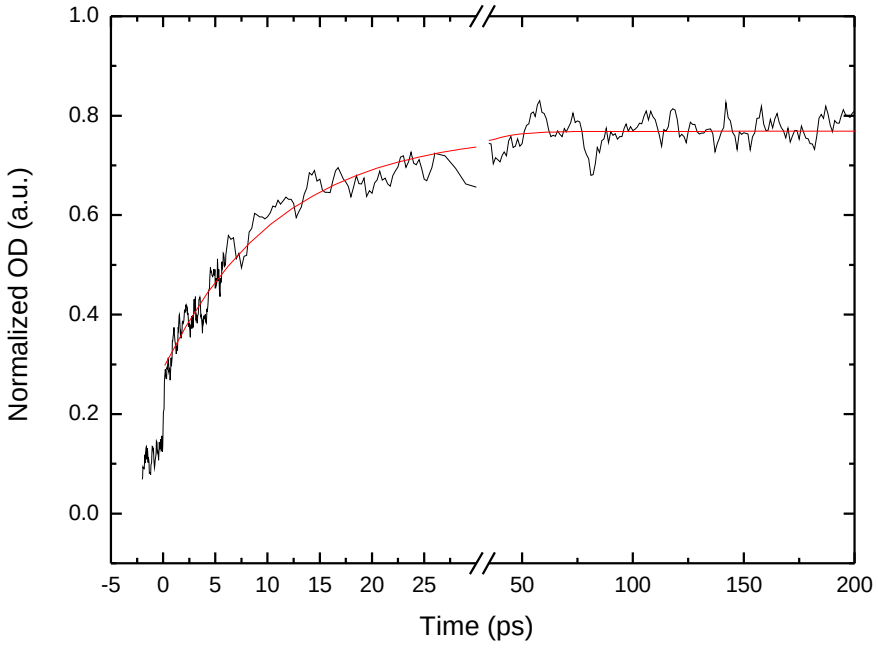

Figure 2.12: Long time window temporal trace of the excited state absorption of ZnO in DN216/ZnO DSSC extracted by taking a horizontal lienout of the transient absorption spectrum in Figure 2.11 at 2160 nm. The trace was found to rise with three time constant of $t_1 = 200$ fs, $t_2 = 2$ ps and $t_3 = 10$ ps.

3. Organic Photovoltaic Cells

Photovoltaic cells are electronic devices developed to convert sunlight to electrical energy, a more accessible form of energy for human usage. The light incident on the photon absorbing component of a photovoltaic cell excites its molecules and creates electron-hole pairs that are subsequently separated into free charge carriers. The electrodes of the cell then harvest the free charge carriers resulting in the flow of the photocurrent through the external circuit. The number of various types of photovoltaic cells available on the market is increasing due to the introduction of new materials and manufacturing techniques. The two main characteristics to compare the performances of the different types of photovoltaic cells are the lifetime and power conversion efficiency.

Photovoltaic cells based on silicon inorganic semiconductors have been the most in use type of photovoltaic cells so far. The efficiency of these devices has already reached 25.6% [4; 5], justifying their market dominance. However, for few decades now organic photovoltaic cells (OPVCs) have been attracting attention among scientists and market suppliers. The recorded efficiency of OPVCs has already reached 11.5% for the all-organic PVCs and 11.9% for the hybrid organic/inorganic PVCs known as dye sensitized solar cells (DSSC) [5]. Photovoltaic cells utilizing organic light absorbers, in general, are known for their low manufacturing cost and high absorption coefficients. Moreover, their abilities to be deposited onto flexible substrates allows for various designs and architectural applications [8]. Research has been focused on studying and understanding the photoinduced processes occurring within OPVCs in order to improve their efficiency and life time.

The main components in the all-organic photovoltaic cells are one or two organic semiconductors deposited as a blend or layers in between two conducting electrodes [9]. The organic materials are the light absorbers and the sources of the strongly bound electron-hole pairs known as excitons. In photovoltaic devices utilizing two organic semiconductors, first introduced by Tang [23], the free charge carriers are created upon the diffusion of excitons to either the organic/organic interface or to the organic/electrode interface where they dissociate. The free charge carriers then propagate to the electrodes to be extracted to the external circuit generating the photocurrent.

The organic/organic interface at which excitons dissociate, in the all-organic PVCs, is known as the donor/acceptor heterojunction. This nomenclature is based on the fact that the acceptor is a material of strong electron affinity that conducts electrons whereas the photoexcited donor is a hole conducting material. The process of light harvesting in these OPVCs starts by the absorption of photons by the donor material (D), as illustrated in Figure 3.1. The electrons of the donor are then excited from their highest occupied molecular orbital (HOMO) to their lowest unoccupied molecular orbital (LUMO), leaving their corresponding holes at the HOMO. Driven by the differences in ionization potential and electron affinity between the donor and the or-

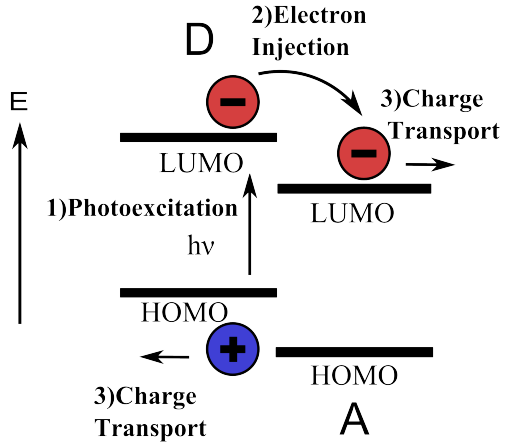

Figure 3.1: The energy diagram of a donor/ acceptor heterojunction. 1) The excitation of an electron from the HOMO of the donor(D) to its LUMO upon photon absorption. 2) The injection of the electron from the LUMO of the donor(D) to the LUMO of the acceptor(A). 3) Transport of the free electron and hole to the electrodes through the acceptor and donor materials respectively.

ganic acceptor material (A), electrons are then injected from the LUMO of the donor to the energetically favourable LUMO of the acceptor. The energy difference is used to free the charges by overcoming the Coulomb attraction potential of the electron-hole pair. After this exciton dissociation has taken place, electrons will propagate through the acceptor (the electron transport medium) to the negative electrode; whereas holes will propagate through the donor material (the hole transport medium) to the positive electrode. When the donor/acceptor heterojunction is structured as a blend such that exciton dissociation occur all along the volume of this blend, the cell is called bulk heterojunction OPVC. But, when the interface has a layered structure where exciton dissociation is localized at the surface between the donor and the acceptor layers, the cell is a planar or thin film heterojunction OPVC [24].

Another OPVC based on an organic light absorber is the dye sensitised solar cell (DSSC) invented by O'Regan and Grätzel [25; 10; 26]. The light absorber and electron donor in this family of solar cells is a monolayer of an organic dye absorbed into the porous surface of a thin film of an inorganic metal oxide semiconductor that acts as the electron acceptor. This OPVC has a somewhat similar working principles to the all-organic PVC. Light harvesting also starts by the excitation of electrons from the HOMO of the dye to its LUMO, as a result of the absorption of the photons. Electrons are then injected into the conduction band of the semiconductor (the acceptor) to be extracted into the external circuit. Various designs of dye sensitized solar cells utilizing different organic dyes and metal oxide semiconductors have been developed over the years since the first Grätzel cell.

The processes of photoinduced exciton generation, charge separation or injection into the transporting media, charge transport to the electrodes and charge extraction by the electrodes should all occur on an ultrafast time scale to win the battle against the competing charge loss mechanisms. These losses are due to relaxation of photoexcited electrons of the light absorber into its ground state as well as radiative and nonradia-

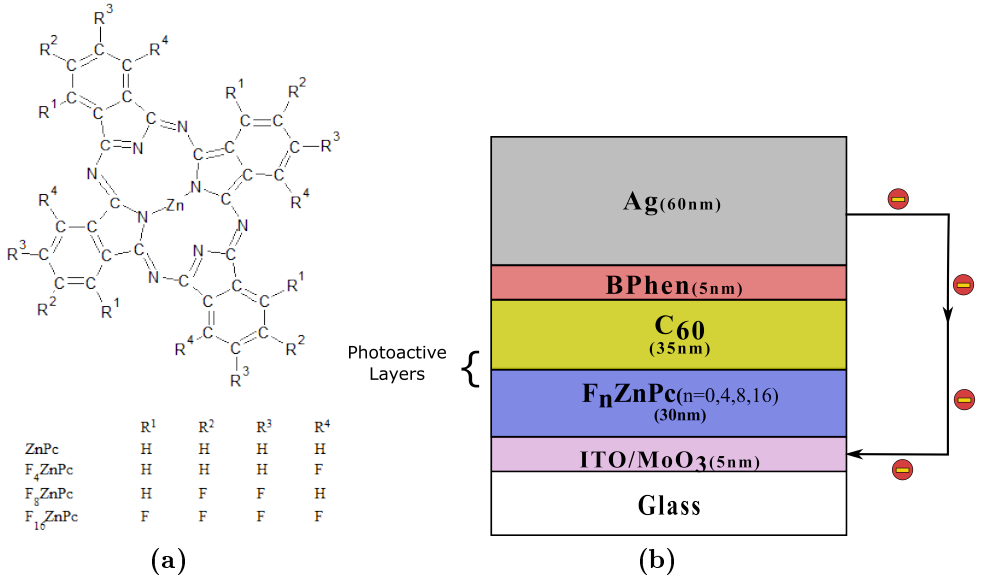

Figure 3.2: (a) The chemical structure and the respective ligand configurations of fluorinated zinc phthalocyanine (F_nZnPc) n=0, 4, 8, 16. (b) Schematic of the layered structure of the performance optimized F_nZnPc/C_{60} cells showing the thickness of each layer. The light absorbing layers are the fluorinated phthalocyanine (F_nZnPc) and the C_{60}, Bathophenanthroline (BPhen) is the exciton blocking layer, the silver layer is the top cathode and the anode is a layer of molybdenumoxide (MoO_3) and Indium tin oxide (ITO).

tive recombinations.

Pump-probe femtosecond transient absorption spectroscopy has been identified as the experimental technique to investigate the photoinduced charge dynamics within solar cells in real time. In this chapter fluorinated Zinc phthalocyanine evaporated organic photovoltaic cells (F_nZnPc/C_{60}, $n = 0, 4, 8, 16$) and Indoline dye DSSC utilizing ZnO as a semiconductor (DN216/ZnO) are presented as two examples of OPVCs where the charge dynamics have been investigated using our newly developed pump near infrared probe transient absorption spectroscopy setup. An introduction to the structure and operation of these two OPVCs as well as the results obtained in our laboratory will be given in the following sections.

3.1 Fluorinated Zinc Phthalocyanine F_nZnPc ($n = 0, 4, 8, 16$) Bilayer Photovoltaic Cells

Cell Structure and Operation

The organic photovoltaic cell presented in this work is a planar heterojunction cell where the electron acceptor is a fullerene C_{60} molecule and the donor is a fluorinated Zinc phthalocyanine. Four photovoltaic cells were fabricated and macroscopically characterized by Michael Brendel [2] at Julius-Maximilians University, Würzburg, Germany. All four cells have a Zinc (Zn) central metal atom of their phthalocyanine but differ in the degree of fluorination i.e the number of fluorine atoms replacing the hydrogen atoms at the ligands of the phthalocyanine. As shown in Figure 3.2(a) the configura-

tion of the donor fluorinated zinc phthalocyanine molecules in each of the four cells is F_nZnPc with $n = 0, 4, 8, 16$.

The layered structure of the cells is sketched in Figure 3.2(b). Each of these cells was prepared on an Indium tin oxide (ITO) coated glass substrate on top of which a 5 nm layer of molybdenumoxide (MoO_3) was added to serve as the hole transport medium (HTM). Above it a 30 nm layer of F_nZnPc, $n = 0, 4, 8, 16$ was deposited to serve, as mentioned earlier, as the electron donor. The electron acceptor is a 35 nm layer of C_{60}. A 5 nm layer of Bathophenanthroline (BPhen) was used as an exciton blocking layer and finally a 60 nm layer of silver (Ag) as the cathode.

Phthalocyanine has been used as a donor and a hole conducting medium since the first bilayer photovoltaic cell developed by Tang [23]. It is known to be flexible for chemical substitutions, by either changing the central metal atom or the hydrogen atoms at the ligand, without severe changes in its structure. Replacing the hydrogen atoms at the ligand of Zinc phthalocyanine molecules (F_nZnPc, $n = 0, 4, 8, 16$) with the more electronegative fluorine atoms has already been proven, in the work done by Mayer *et al.* [27] to shift the positions of the HOMO and LUMO levels without changing the gap between these energy levels. The systematic adjustment of the position of the energy levels of the donor has been recognized as an efficient method to understand the properties of the donor/acceptor heterojunction and its dependence on the microscopic properties of the photoactive materials [24]. Zinc phthalocyanine (ZnPc) in combination with C_{60} as an acceptor is known for its good absorption and charge transport properties as well as high short circuit current density (J_{sc}) and fill factor (FF) [28]. However, this donor/acceptor combination suffers from low open circuit voltage (V_{oc}): a photovoltaic quantity that is directly related to the effective energy gap ($E_{g,eff}$) between the HOMO of the donor and the LUMO of the acceptor [2]. Fluorinating zinc phtalocyanine with four fluorine atoms F_4ZnPc has already been proven to shift the ionization potential of the molecule upwards resulting in an increase in the V_{oc} of a bulk heterojunction OPVC sensitized with a C_{60} molecule as an electron acceptor [28].

In the work done by Brendel *et al.* [2] the effect of gradual fluorination on the physical properties of F_nZnPc ($n = 0, 4, 8, 16$) thin films and F_nZnPc/C_{60} bilayer cells was investigated. Spectrally resolved photoluminescence, absorption and X-ray diffraction measurements (XRD) were performed on 40 nm thin films of F_nZnPc on glass substrates to study the effect of gradual fluorination on the optical band gap and structural properties of the phthalocyanines. Measurements on the cell parameters: the open circuit voltage (V_{oc}), the short circuit current density (J_{sc}), the fill factor (FF) and the efficiency (η) were done using the performance optimized F_nZnPc/C_{60} cells.

Furthermore, Brendel *et al.* [2] performed thickness-dependent ultraviolet photoelectron spectroscopy (UPS) measurements on F_nZnPc/C_{60} cells to compare the shift in the HOMO and LUMO positions of each of the phthalocyanines as a result of the gradual fluorination. In this experimental technique the kinetic energy and the number of photoelectrons generated after bombarding a sample with photons in the ultraviolet spectral range are recorded using an electron spectrometer. The binding energy of an ejected photoelectron is equal to the energy of the incident photon minus recorded

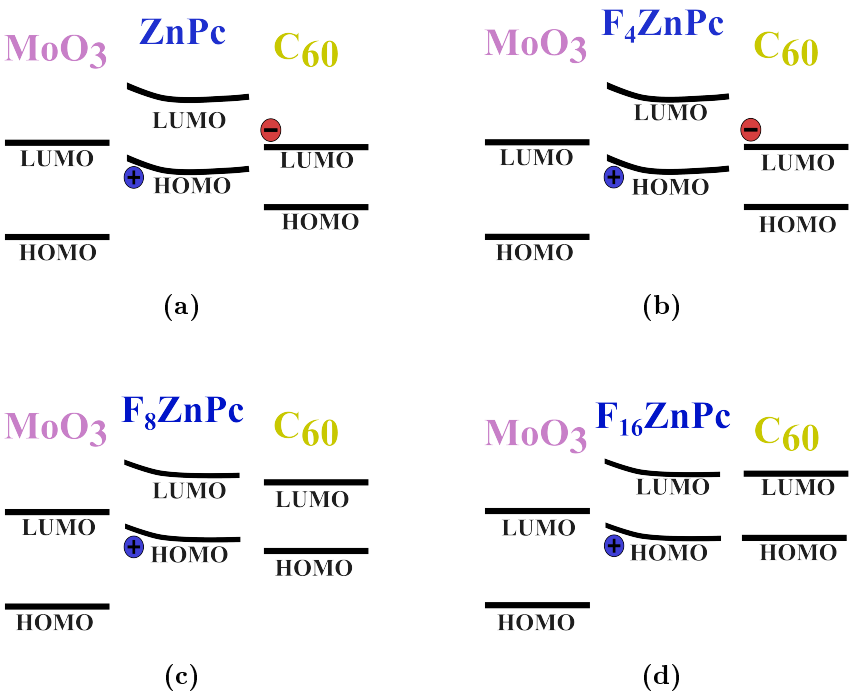

Figure 3.3: A schematic of the energy levels of F_nZnPc/C_{60}, $n = 0, 4, 8, 16$ ((a)-(d) respectively). The energy differences ΔE_{LUMO} and ΔE_{HOMO} decrease as the degree of fluorination increases.

kinetic energy of the photoelectron[29]. The spectrometer represents the results in a plot of the relative number of photoelectrons versus their binding energy. The peaks in this plot indicate energy shells and the peak with the least binding energy is the valance band. The onset of the peak and not its maximum determines the value of the binding energy of the valance band with respect to the Fermi level.

A model of the band structure of the F_nZnPc/C_{60} ($n = 0, 4, 8, 16$) planar heterojunction devices was formulated based on the results of the UPS measurements on the active organic layers. The band structure for the four devices is summarized in Figure 3.3. As a common feature, all four cells show a strong Fermi level pinning of their HOMO levels at the interface with MoO_3; that is the position of the HOMO of the phthalocyanine with respect to the Fermi level is higher at the interface than at 30 nm thickness. This effect appears in the diagram as an upward bending of the HOMO of all four devices at the interface with the MoO_3. This effect occurs as a result of the accumulation of the positive charge at the surface of the MoO_3 due to its high work function. The properties of the energy levels at the donor/acceptor interface, however, differs in the four devices. The HOMO of the ZnPc and F_4ZnPc shift upward after the deposition of the C_{60} layers. The C_{60} shows a LUMO pinning that causes the negative charge to accumulate at its surface. The electric field between the negative charge accumulated at the donor/acceptor interface and the positive charge at the phthalocyanine/MoO_3 interface causes the HOMO of the ZnPc and F_4ZnPc to bend upwards. As for the other two phthalocyanine bilayer devices (F_8ZnPc/C_{60} and F_{16}ZnPc/C_{60}) the fullerene shows no LUMO pinning. The C_{60} LUMO pinning at the interface with the ZnPc

and F_4ZnPc is attributed to the fact that the acceptor molecule has a higher electron affinity than the ionization potential of the donor. Whereas in the F_8ZnPc/C_{60} and F_{16}ZnPc/C_{60} cells the effective energy gap $E_{g,eff}$ is not sufficient for the accumulation of the charge to occur and consequently the C_{60} LUMO pinning.

In all four planar heterojunction devices (PHJ) both the C_{60} and the F_nZnPc ($n = 0, 4, 8, 16$) photoactive layers absorb photons and generate excitons. To conclude on the contribution of each of these two layers to the photogeneration of charge carriers, [2] calculated the wavelength-dependent external quantum efficiency (EQE) for each of the four cells. EQE is the ratio of the extracted charge carriers to the number of incident photons. An increment of 25% in the EQE of F_4ZnPc/C_{60} in comparison with the nonfluorinated ZnPc. In contrast, the EQE of F_8ZnPc/C_{60} and that of F_{16}ZnPc/C_{60} decrease by 70% and 60%, respectively. These results are explained by the different exciton dissociation mechanisms in these devices due to different energetics at the donor/acceptor interface upon fluorination.

In ZnPc/C_{60}, F4ZnPc/C_{60} and F8ZnPc/C_{60} excitons, upon photogeneration within either the phthalocyanine or the fullerne, propagate to the donor/acceptor interface to dissociate. The dissociation of the excitons generated at the phthalocyanine is driven by the energy difference between the LUMO of the F_nZnPc ($n = 0, 4, 8$) and the LUMO of the C_{60} (ΔE_{LUMO}). Whereas the driving potential for the dissociation of the C_{60} molecule is the HOMO of the F_nZnPc ($n = 0, 4, 8$) and the HOMO of the C_{60} (ΔE_{HOMO}). The energy difference ΔE_{LUMO} exceeds the exciton binding energy of the phthalocyanines in the ZnPc/C_{60} and F_8ZnPc/C_{60} cells therefore, exciton dissociation is efficient. The F_8ZnPc/C_{60} cell is less efficient regarding exciton dissociation because the energies ΔE_{HOMO} and ΔE_{LUMO} are of the same level as the exciton binding energies of the C_{60} and the phthalocyanine. As for the fourth cell F_{16}ZnPc/C_{60} the energies ΔE_{LUMO} and ΔE_{HOMO} are less than the exciton binding energies of the light absorbing materials, therefore, no exciton dissociation takes place at the donor/acceptor interface. The fact that the EQE measurements still show a non-zero photocurrent from these cells suggests that they have a different working principle compared to the other F_nZnPc/C_{60} ($n = 0, 4, 8$) cells [2]. Upon photogeneration excitons propagate to the interface with the MoO_3 positive electrode and not to the donor/acceptor interface to dissociate.

To develop a better understanding of the working principle and the charge dynamics within the four F_nZnPc/C_{60} ($n = 0, 4, 8, 16$) cells, pump-probe femtosecond transient absorption spectroscopy (TAS) measurements were performed in our laboratory using the experimental setup presented in Chapter 2.

Figure 3.4 shows the steady state absorption spectra of the four F_nZnPc/C_{60} ($n = 0, 4, 8, 16$) cells and a thin film of pure C_{60}. The absorption in the range 400 - 550 nm is mainly due to the C_{60} molecule whereas the absorption in the range 550 - 850nm is assigned to the fluorinated phthalocyanines [2]. As can be seen in the figure, all three phthalocyanines ZnPc, F_4ZnPc, F_8ZnPc have similar absorption spectra with two maxima, one around 600 nm (indicated by the red vertical line) and the other at 700 nm (indicated by the green vertical line). The peak around 600 nm is red shifted for

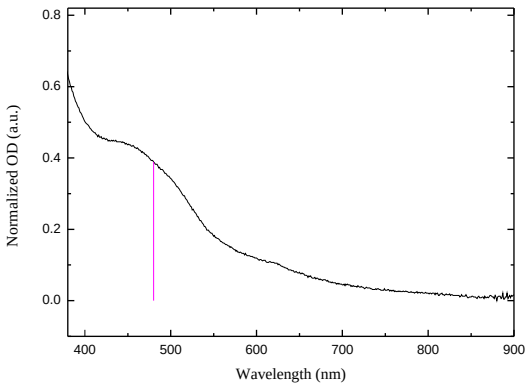

(a) C_{60}

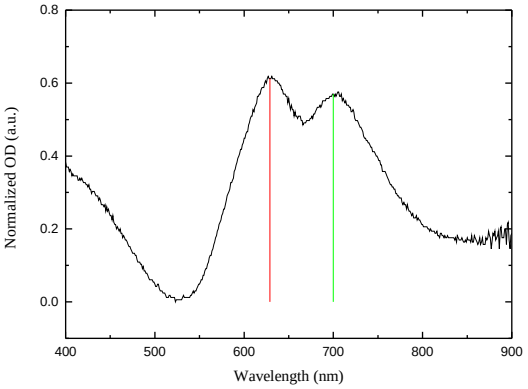

(b) ZnPc

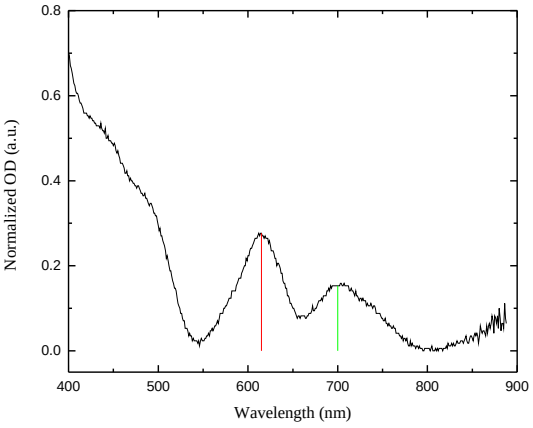

(c) $ZnPc/C_{60}$

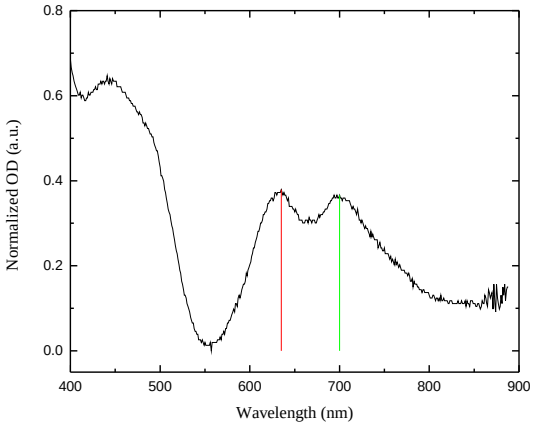

(d) F_4ZnPc/C_{60}

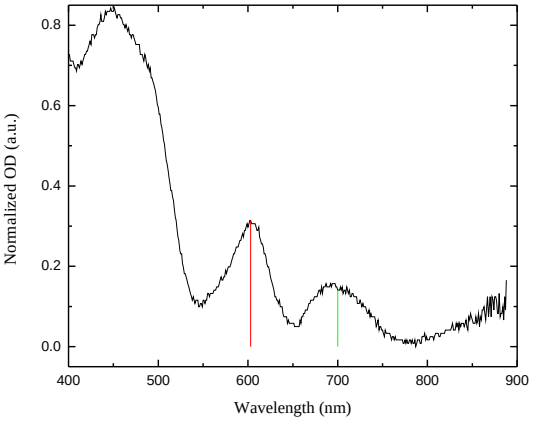

(e) F_8ZnPc/C_{60}

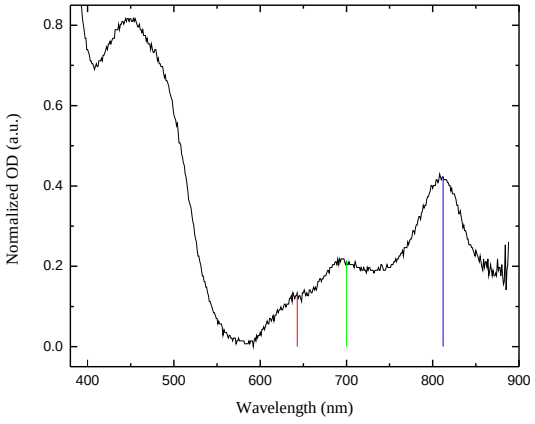

(f) $F_{16}ZnPc/C_{60}$

Figure 3.4: Steady state absorption spectra of (a) pure C_{60} thin film, (b) a thin film of ZnPc and (c), (d), (e), (f) F_nZnPc/C_{60} ($n = 0, 4, 8, 16$) OPVCs.

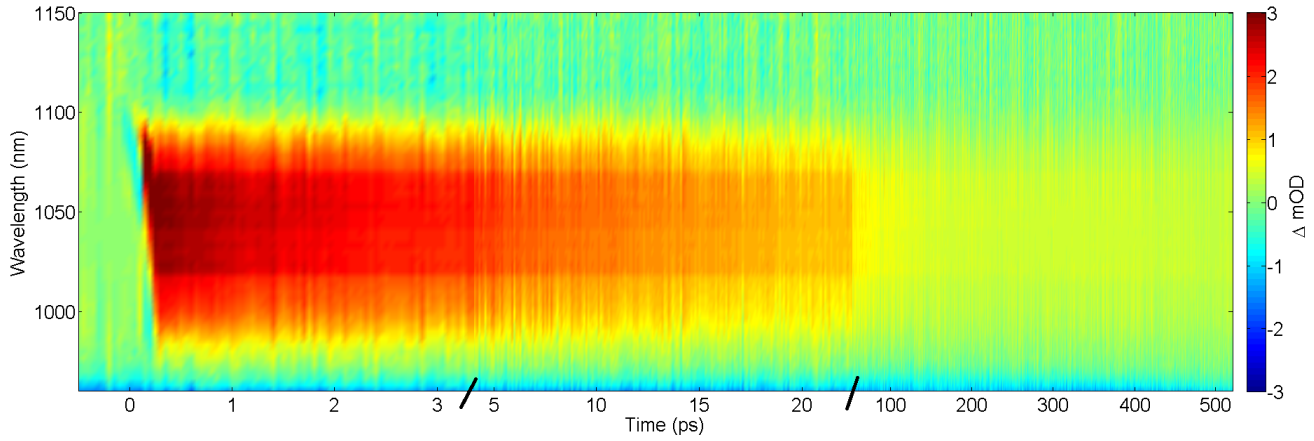

Figure 3.5: The long time window NOPA pump- NOPA probe transient absorption spectrum of ZnPc/C_{60} in 50 fs, 100 fs and 1 ps time steps. The central wavelength of the pump pulse was set to 480 nm and the probe's to 1050 nm.

the F_4ZnPc in comparison with the peak of the ZnPc whereas the peak for the F_8ZnPc is blue shifted. The similarity in the absorption spectra indicate the stability of the optical band gap upon fluorination and also crystallographic symmetry, whereas the shift in the absorption maxima, although small, indicate modification in the transition dipole alignment and intermolecular coupling [2]. F_{16}ZnPc has a different absorption spectrum; in addition to the two peaks similar to the other phthalocyanines, it has a third absorption maximum around 815 nm. The maximum around 600 nm is blue shifted in comparison to the non fluorinated phthalocyanine. These spectral differences of F_{16}ZnPc, with respect to the other fluorinated phthalocyanines, are attributed to the different intermolecular packing due to different structures [2].

Femtosecond Transient Absorption Spectra

The pump probe femtosecond transient absorption (TA) spectroscopy experimental setup described in Chapter 2 was used to detect the charge dynamics within the four fluorinated zinc phthalocyanine F_nZnPc/C_{60} ($n = 0, 4, 8, 16$) solar cells. Moreover, TA measurements were carried out on thin films of F_nZnPc ($n = 0, 4, 8, 16$) as well as on thin film of pure C_{60} for comparison.

TA measurements were also performed on the F_nZnPc/C_{60} ($n = 0, 4, 8, 16$) with a pump central wavelength of 700 nm, a common maximum absorption value for all four phthalocyanines as indicated by the steady state absorption spectra shown in Figure 3.4. A white light continuum produced in a Yttrium aluminium garnet (YAG) crystal was used to probe the cells in the visible spectral range 450 - 700 nm. TA measurements were also carried out using the YAG crystal in the near infrared range 900 - 1400 nm. TA measurements on F_nZnPc/C_{60} ($n = 0, 4, 8, 16$) cells were also performed using a pump of central wavelength of 480 nm. This wavelength value corresponds to a maximum absorption of the fullerene C_{60} where the contribution of the absorption of the phthalocyanines F_nZnPc ($n = 0, 4, 8, 16$) is negligible. A negative TA measurement (i.e no absorption signal was detected) was done on F_{16}ZnPc thin film to confirm that the

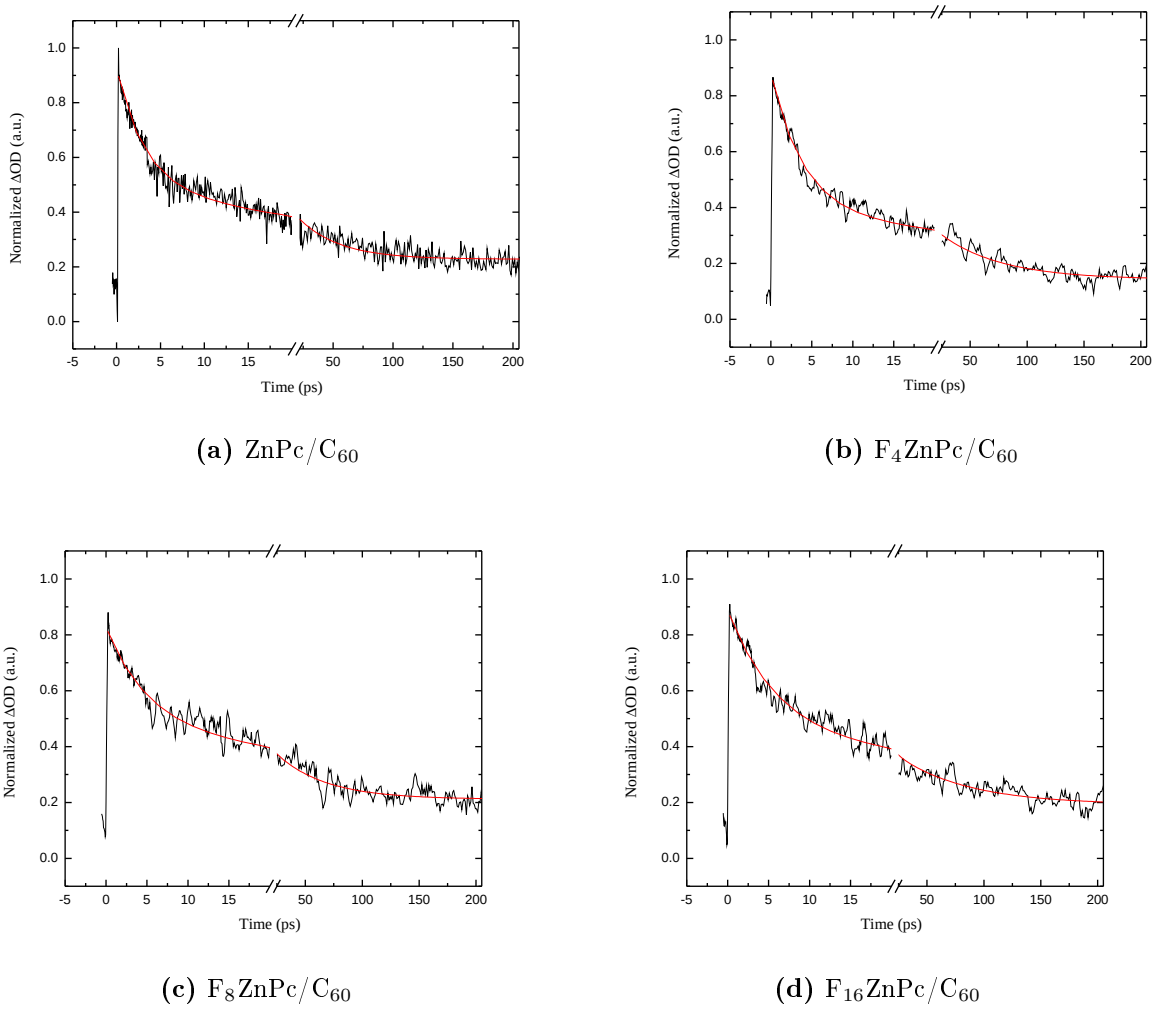

(a) $ZnPc/C_{60}$ **(b)** F_4ZnPc/C_{60}

(c) F_8ZnPc/C_{60} **(d)** $F_{16}ZnPc/C_{60}$

Figure 3.6: The decay trace of the C_{60}^- anion taken at 1050 nm from the long time window scan of the transient absorption spectra of the F_nZnPc/C_{60} $(n = 0, 4, 8, 16)$ cells.

absorption signal observed when exciting at 480 nm is only due to the C_{60} excitation. The motive behind these two sets of measurements (pump at 480 nm and 700 nm) was to detect the dissociation of excitons generated in the two absorber materials: F_nZnPc $(n = 0, 4, 8, 16)$ and C_{60}, in all four cells. Using these two pump pulses, independent excitation of the two absorber materials was insured.

As a result of the dissociation of excitons generated within the fluorinated zinc phthalocyanines F_nZnPc $(n = 4, 8, 16)$, electrons are injected into the fullerene C_{60} layer generating C_{60}^- anions. These charged species can also be generated by direct photoexcitation of the C_{60} due to autoionization. In this intramolecular process an electron is transferred from the excited C_{60} molecule to a neighbouring molecule. The C_{60}^- anion is considered a charge transfer state that proceeds the generation of free charge carriers in the C_{60} layer [30]. The absorption at 1050 nm is assigned to this C_{60}^- anion [31; 22]. TA measurements using a noncollinear optical parametric amplifier (NOPA) idler signal as a probe were carried out on the F_nZnPc/C_{60} cells to investigate the excited state

Table 3.1: A summary of the time constants extracted by fitting the lineouts shown in Figure 3.6.

Photovoltaic Cell	t_1 (ps)	t_2 (ps)
ZnPc/C_{60}	3	34
F_4ZnPc/C_{60}	4	52
F_8ZnPc/C_{60}	4	37
F_{16}ZnPc/C_{60}	5	45

absorption observed at 1050 nm. The long time window transient absorption spectrum of the ZnPc/C_{60} pumped at 480 nm and probed at 1050 nm using the idler of the noncolinear optical parametric amplifier (NOPA) is shown as an example in Figure 3.5. As also observed for the F_nZnPc/C_{60} ($n = 4, 8, 16$) cells a decaying absorption signal was observed.

Figure 3.6 shows the horizontal lineouts extracted from the long time window transient absorption spectra of the four F_nZnPc/C_{60} ($n = 0, 4, 8, 16$) samples. Fitting the extracted traces, the time constants related to the decay of the absorption signal of the C_{60}^- anion were extracted. All four lineouts were fitted with a biexponential function and the two time constants extracted for each of the four samples are summerized in Table 3.1.

The recombination of the electrons of the C_{60}^- anion is believed to be a trap assisted process [32]. This means that the recombination of electrons with holes is a two steps process where electrons are first captured by trap states, that can be created due to impurities of the material, before relaxing into the ground state [33]. Therefore, the short time decay (4 ps $\pm$ 1 ps) of the absorption signal in all F_nZnPc/C_{60} ($n = 0, 4, 8, 16$) cells is attributed to the electrons of C_{60}^- anion being captured by trap states within the bulk of the C_{60} layer whereas the long time decay (43 ps $\pm$ 9 ps) is due to electrons being captured by trap states existing at the surface of the C_{60} layer with air.

Figure 3.7 shows the short time window transient spectra of the F_nZnPc/C_{60}s . These spectra were taken in 15 fs time steps to compare the rise time of the C_{60}^- absorption signal for all four samples. How fast the absorption signals appear on the transient spectrum of each of the four samples, indicate the speed by which the anion was formed. Figure 3.8 shows the horizontal lineouts extracted at 1050 nm from the short time scans. Within the setup temporal resolution, the four differently fluorinated cells show the same ultrafast rise time, $\sim$ 150 fs, for the absorption signal at 1050 nm. This indicates that the absorption of the C_{60}^- anion is independent of the energetics at the donor/acceptor heterojunction. The sub 150 fs rise time of the absorption signal also indicates that the newly generated probe pulse duration must be less than 150 fs, keeping in mind that the pump pulse duration was 50 fs. A more detailed study on the duration of this pulse is presented in Chapter 4.

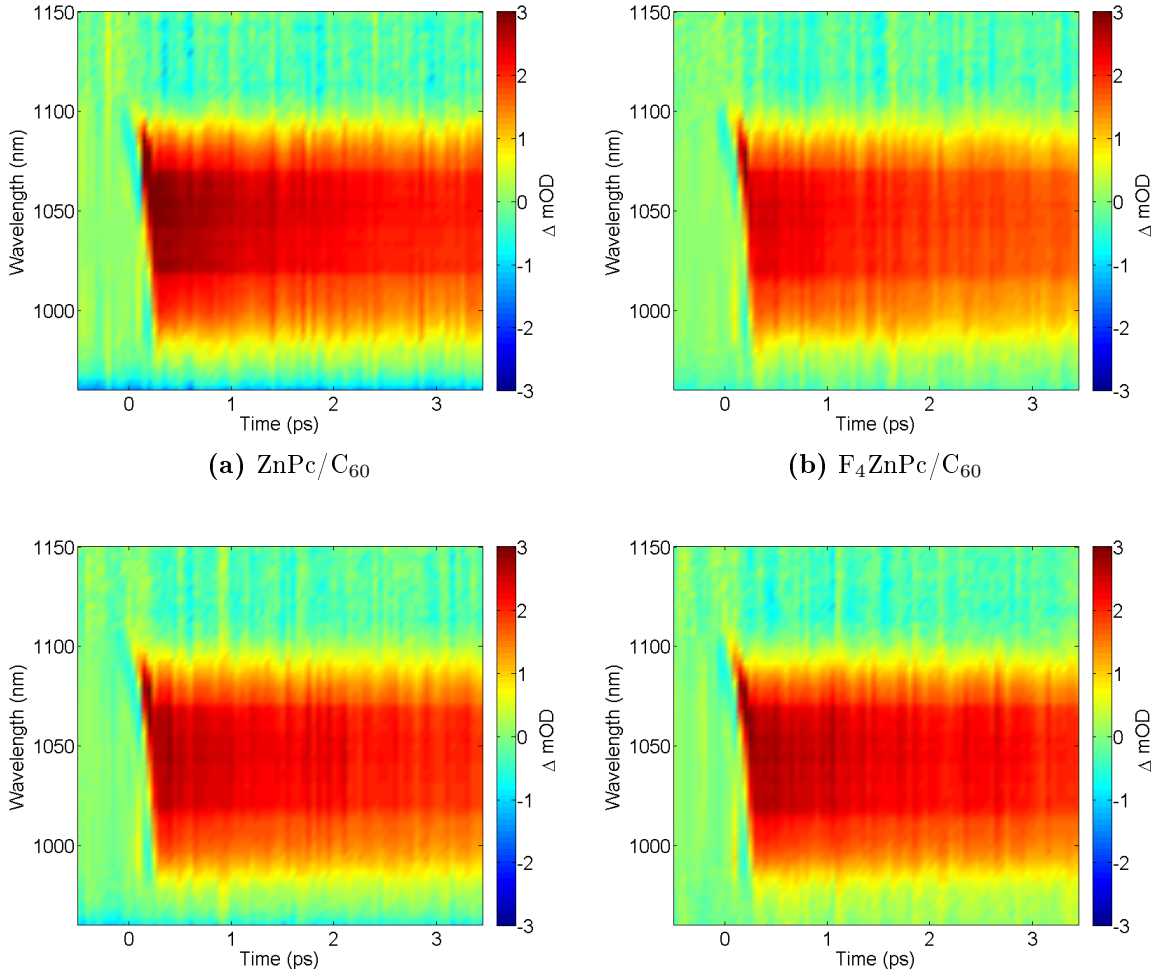

(a) $ZnPc/C_{60}$ **(b)** F_4ZnPc/C_{60}

(c) F_8ZnPc/C_{60} **(d)** $F_{16}ZnPc/C_{60}$

Figure 3.7: The NOPA pump- NOPA near infrared probe short time window transient absorption spectra of the F_nZnPc/C_{60} $(n = 0, 4, 8, 16)$ taken in 15 fs time steps. The pump pulse was centered around 480 nm and the probe around 1050nm.

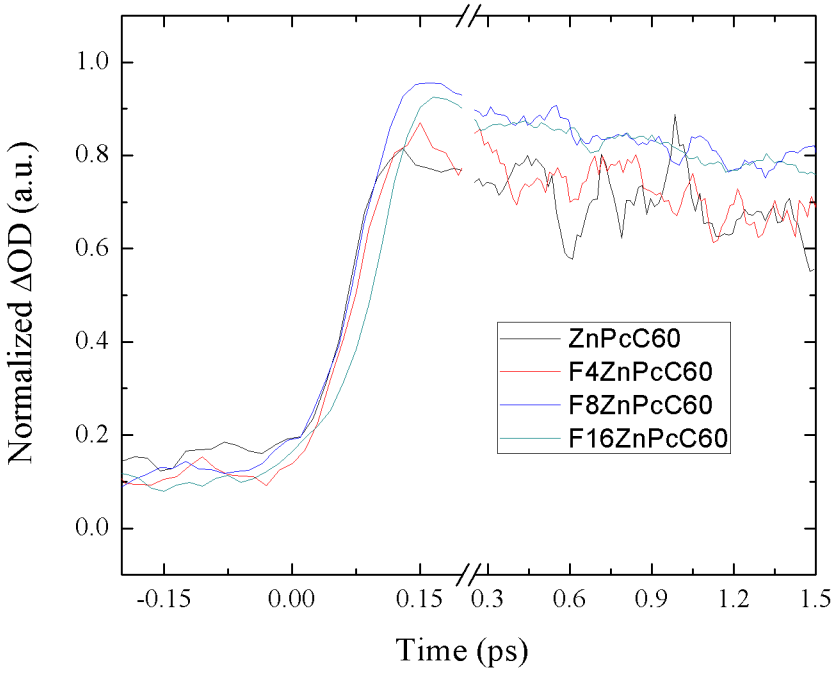

Figure 3.8: Temporal traces of the C_{60}^{-} absorption in F_nZnPc/C_{60} ($n = 0, 4, 8, 16$) extracted from the transient absorption spectra shown in Figure 3.7. The rise time of this signal is similar for all four cells.

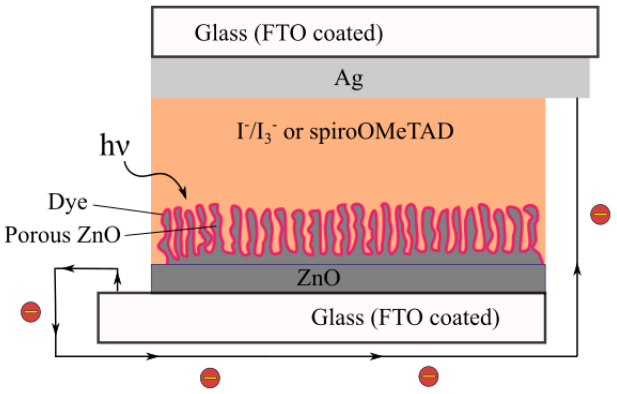

Figure 3.9: Schematic of the layer structure of the indoline D216/ZnO dye sensitized solar cell. The light absorber is a monolayer of the dye that is porously adsorbed into the surface of the ZnO semiconductor. The anode is a packed layer of ZnO deposited on an FTO coated glass substrate. The is silver on FTO coated glass and the circuit is closed with either an I^-/I_3^- in electrolyte solution or spiroOMeTAD.

3.2 Indoline dye sensitised solar cells

Cell Structure and Operation

The DSSC studied in this work, as can be seen in Figure 3.9, is based on a nanoporous zinc oxide(ZnO) semiconductor sensitized by the indoline dye derivative DN216 [34; 1]. The cell was prepared by Iulia Minda [35] on a fluorine-doped-tin oxide (FTO) coated glass substrate. On top of the substrate a tightly packed layer of ZnO was electrodeposited to serve as a hole blocking layer. A nanoporous ZnO layer was deposited on top of the packed ZnO layer, then a monolayer of the indoline dye DN216 was adsorbed onto its surface. The porous structure of ZnO has a high surface area that insures an efficient coupling between the dye and the semiconductor. The hole transport medium (HTM) in this cell was either an iodide/triiodide redox couple in electrolyte solution or the solid state organic hole conductor 2,2′,7,7′-tetrakis-(N,N-di-p-methoxyphenyl-amine)-9,9′-spirobifluorene (spiro-OMeTAD) spin coated as a solution onto the substrate. The cathode is Silver (Ag) evaporated onto another FTO coated glass substrate that sealed the cell.

The choice of ZnO as a semiconductor was based on the fact that it has a band gap similar to TiO_2 (the semiconductor used in the original Grätzel cell) and a higher charge mobility and roughness factor. It also requires a low temperature electrodeposition therefore, it contributes to the reduction of the energy payback time of the cell [34]. The choice of the dye was motivated by improving the efficiency of the electron injection into the semiconductor and improving the adsorption into the surface of the semiconductor thereby increasing the life time of the cell [36]. The hole conducting materials used in this cell are a I^-/I_3^- electrolyte solution and a spiro-OMeTAD solid hole conductor. In both materials the regeneration of the dye molecules after the injection of its electrons to the semiconductor is a faster process than the recombination with the electrons in the conduction band of the semiconductor therefore they are regarded as good reducing agents.

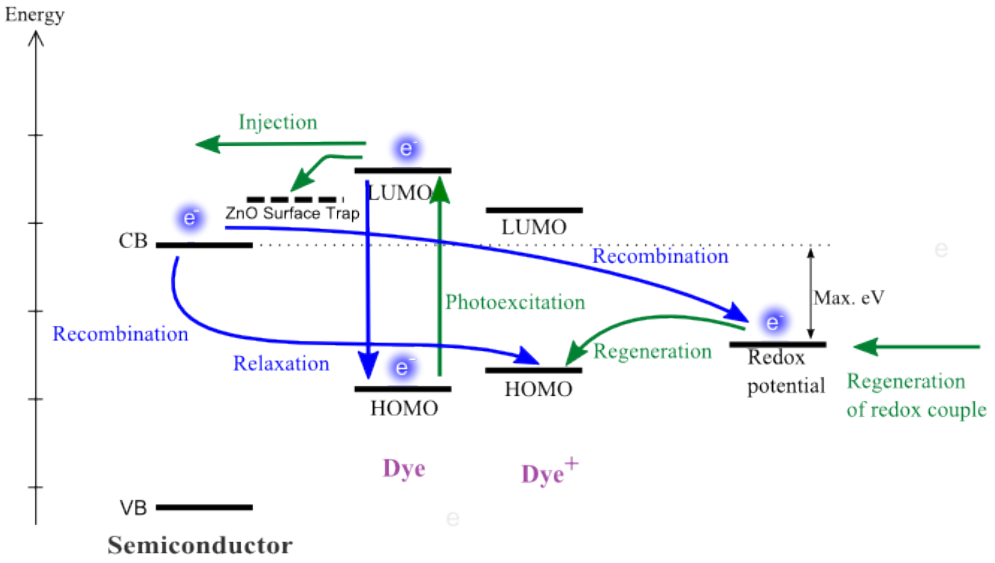

Figure 3.10: Schematic of the energy levels and charge dynamics within a D216/ZnO dye sensitized solar cell utilizing the redox couple I^-/I_3^- in electrolyte solution as a hole transport medium [34].

Figure 3.10 is a reprint of the schematic of the molecular energy levels of the DN216/ZnO dye sensitized solar cell and the charge dynamics within the cell as reported by Rohwer *et al.* [34]. Electrons are excited from the highest occupied molecular orbit (HOMO) of the neutral dye to its lowest unoccupied molecular orbit (LUMO) upon the absorption of photons. The electrons in the LUMO are then injected either directly or via trapped states into the conduction band of the ZnO semiconductor. The dye is then regenerated by either the redox couple I^-/I_3^- or the spiro-OMeTAD. Regeneration of the dye through the reduction of the oxidized dye (Dye^+) by the redox couple was found to be a nanosecond-scale process. In contrast, the dye's regeneration through the injection of holes into spiro-OMeTAd (not shown in the figure) is known to occur immediately after the injection of electrons into the semiconductor [37]. In the optimum case, holes in the hole transport medium (HTM) and electrons in the conduction band of ZnO are transferred to the contact electrodes. A less than optimum performance of the cell is attributed to the relaxation of the electrons from the LUMO of the neutral dye back to its HOMO or to recombination of the electrons in the conduction band of ZnO with either the holes in the oxidized dye or in the HTM. The relaxation and recombination processes are indicated by the blue arrows in the figure.

This model was based on the analysis of the transient absorption (TA) spectrum of the DN216/ZnO DSSC as well as electrochemical measurements and steady state absorption spectrum of the cell. The TA spectrum was measured by Rohwer *et al.* [34] using the pump probe transient absorption experimental setup described in Chapter 2 in the visible spectral region 450 - 700 nm. The central wavelength of the pump pulse was 530 nm, which the maximum absorption value of the dye determined from its steady state absorption spectrum shown in Figure 3.11. This spectrum shows a broad absorption from 500 nm to 600 nm with a peak around 530 nm.

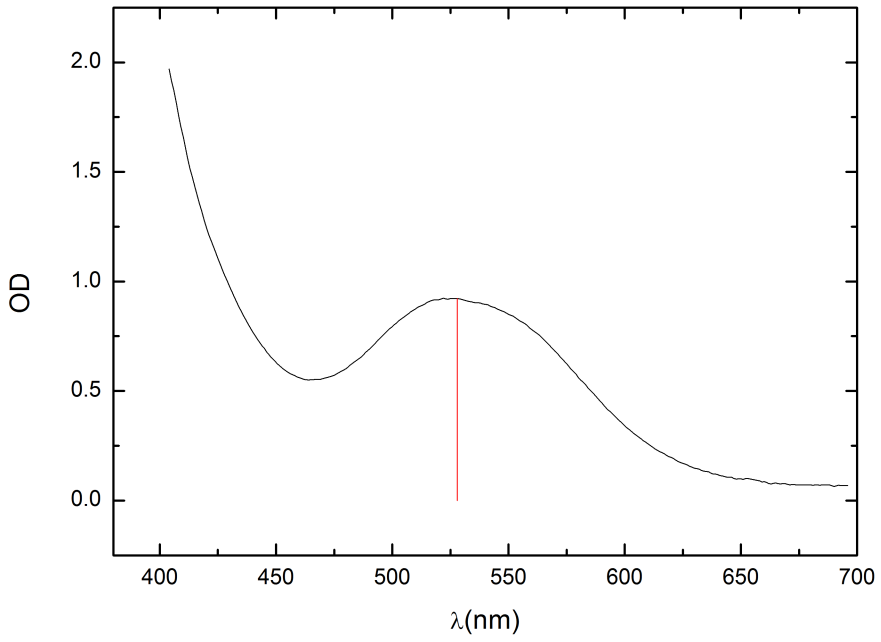

Figure 3.11: The steady state absorption spectrum of the dye sensitized solar cell DN216/ZnO.

The spectral signatures identified in the TA spectrum were assigned by Rohwer *et al.* [34] to the oxidized dye absorption (OX) (below 480 nm), the ground state bleach of the neutral dye (GSB) (500 - 600 nm) and the excited state absorption (ESA) of the neutral dye combined with a contribution from the oxidised dye absorption (abbreviated as ESA+OX)(600 - 700 nm). Using the temporal traces of these signatures the ultrafast direct injection of the electrons from the LUMO of the neutral dye to ZnO conduction band was found to occur in $\sim$ 200 fs as indicated by the decay of the ESA signal and the rise of the OX signal. Electrons were also found to be injected via surface trap state in about 2 ps time scale as again predicted by the decay of the ESA and the rise of the OX. The relaxation of electrons from the LUMO of the neutral dye back to the HOMO in 30 ps as indicated by the rise of the ground state bleach signal as well as a corresponding decay of the ESA signal. A long time constant $>$ 1 ns was detected in the rise of the GSB signal as well as in the decay of the OX signal. This time constant was assigned to the regeneration of the neutral dye as a result of the reduction of the oxidized dye by the HTM. The injection of the electrons into the conduction band of ZnO was concluded from the decay of the ESA signal and the rise of the OX signal but was not directly measured in this study.

In this work a transient absorption (TA) spectrum of the DN216/ZnO DSSC, with both the I^-/I_3^- and the spiro-OMeTAD HTM, was measured in the spectral region of 900 nm to 2400 nm in order to further investigate the injection of the electrons from the excited dye into the semiconductor. Electrons in the conduction band of ZnO are known to absorb light in the near infrared region [38]. Therefore, the near infrared

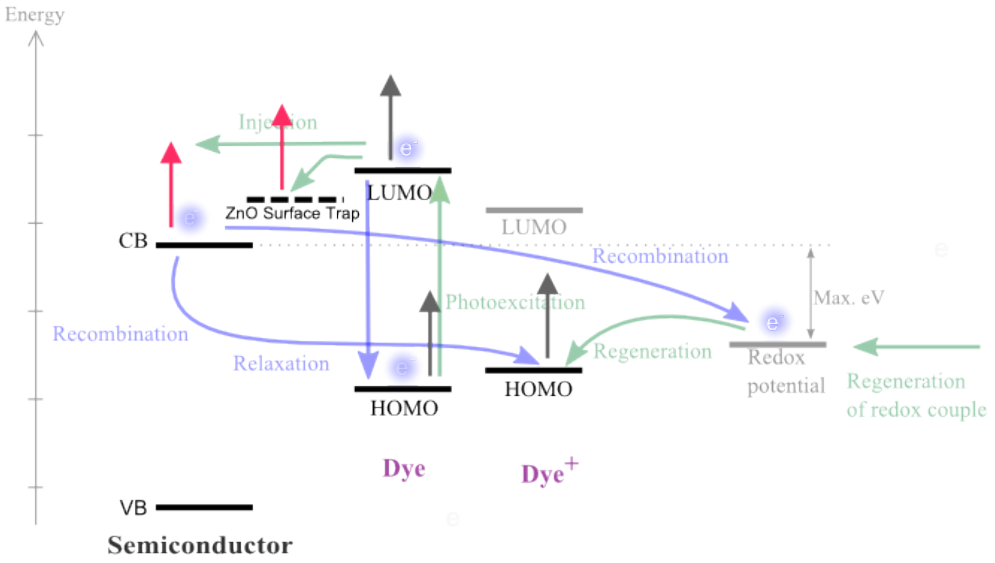

Figure 3.12: The OX, ESA and GSB signals (gray arrows) have already been detected in the work done by Rohwer *et al.* [34], in the spectral range 450 - 700 nm, using a white light continuum. The detection of the electrons in the conduction band of the semiconductor and in the surface trap states (pink arrows) requires a probe light in the near infrared range (900 - 2400 nm).

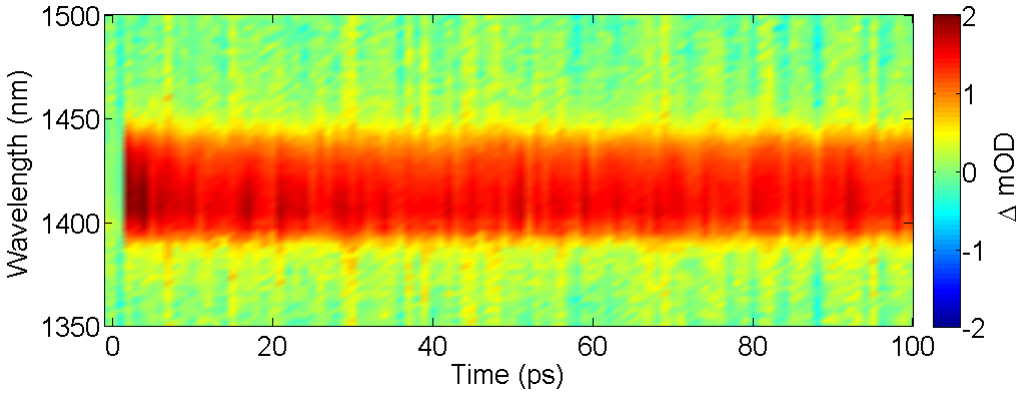

Figure 3.13: The transient absorption spectrum of D216/ZnO DSSC utilizing spiroOMeTAD as a hole conducting medium. The pump is set to 530 nm and the probe central wavelength is 1400 nm.

femtosecond pulses generated from the idler of the NOPA were used as a probe in the transient absorption measurements.

Near Infrared Transient Absorption Spectra of DN216/ZnO DSSC

Near Infrared Probe Spectral Range 900 - 2000 nm

Similar to the measurements in the visible spectral region, the pump pulse was set to the maximum absorption of the DN216 dye of 530 nm central wavelength. The duration of the pump pulse was measured to be sub 50 fs.

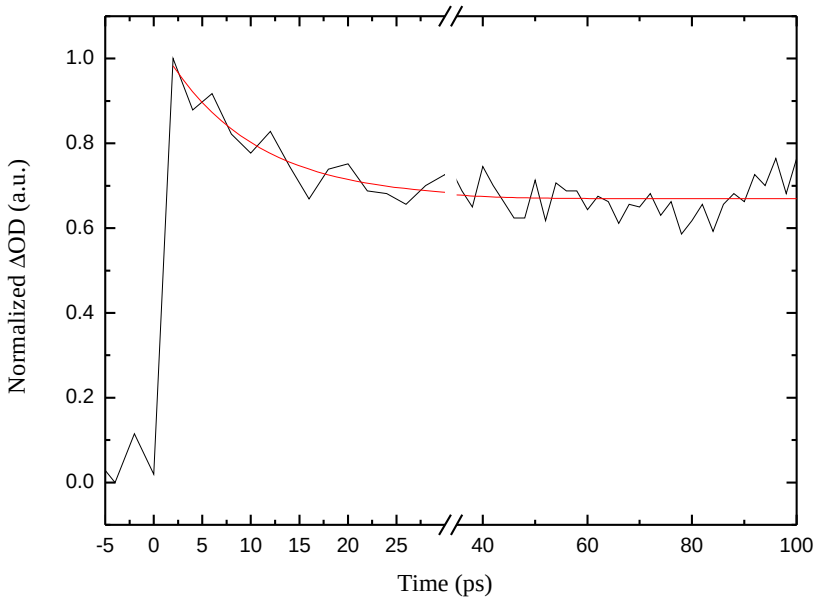

Figure 3.14: Temporal trace extracted at 1435 nm from the transient absorption shown in Figure **??**. The fit (red line) shows that the trace decays with 10 ps time constant.

The probe pulse was tuned gradually between 900 nm and 2000 nm and TA spectra were recorded every 50 nm. An absorption signal was observed in the spectral range 1000 nm to 1400 nm. The long time window transient absorption spectrum of the DN216/ZnO DSSC utilizing spiroOMeTAD as a hole conducting medium with probe wavelength centered around 1400 nm is shown, as an example, in Figure 3.13. A horizontal lineout was extracted from the TA spectrum at 1435 nm. The extracted temporal trace is shown in Figure 3.14. The trace was fitted with a mono-exponential function that decays with 10 ps.

A similar decay constant was obtained for the TA measurements on the DN216/ZnO DSSC utilizing the I^-/I_3^- electrolyte solution as a hole conducting medium in the spectral range 1000 nm to 1400 nm. The absorption in the spectral range 1500 nm to 2000 nm was found to have a different temporal signature. Figure 3.15 shows the TA spectrum of the DN216/ZnO DSSC using the spiroOMeTAD as a hole conducting medium. The probe central wavelength was set to 1650 nm. The temporal trace extracted at 1650 nm from the TA spectrum is shown in Figure 3.16. This signal was found to decay with 2 ps time constant.

Probing electrons in the conduction band of ZnO ($>$ 2000 nm)

The central wavelength of the probe pulse was also gradually tuned in the spectral region 2000 - 2400 nm. Figure 3.17 shows the transient absorption spectrum of the DN216/ZnO DSSC utilizing spiroOMeTAD as an HTM. The probe central wavelength was set to 2160 nm. The horizontal lineout extracted at 2160 nm is shown in Figure

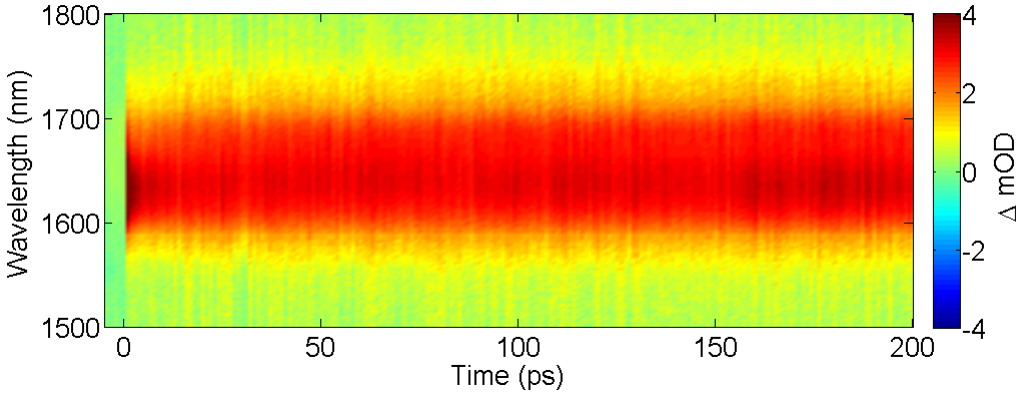

Figure 3.15: The transient abosroption spectrum of D216/ZnO DSSC utilizing spiroOMeTAD as a hole conducting medium. The pump is set to 530 nm and the probe central wavelength was 1650 nm. The spectrum was recorded in 1 ps time steps.

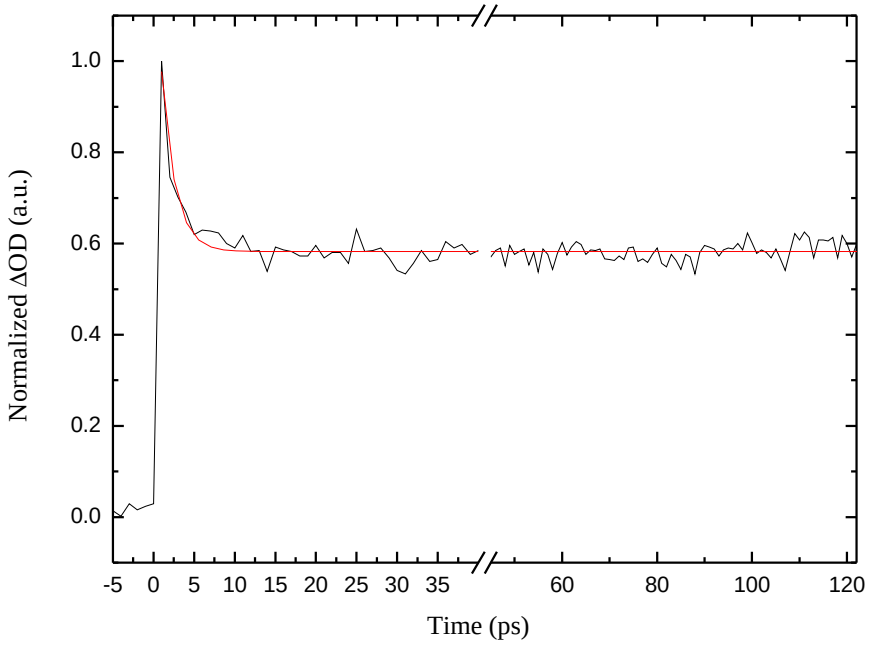

Figure 3.16: Temporal trace extracted at 1650 nm from the transient absorption shown in Figure 3.15. This absorption signal was found to decay with 2 ps time constant.

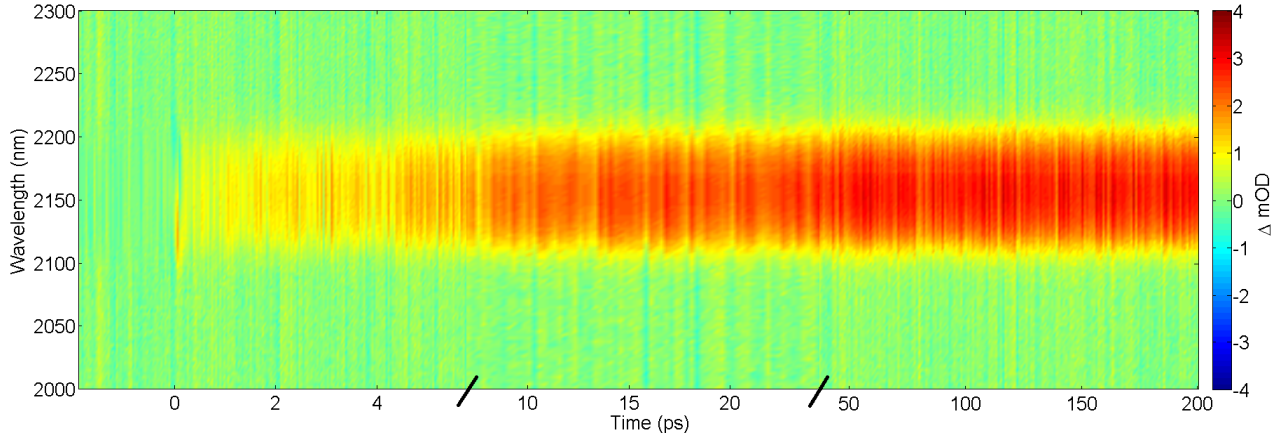

Figure 3.17: Transient absorption spectrum of the indoline dye DN216/ZnO DSSC with spiroOMeTAD as a hole conducting medium. The probe is centered around 2160 nm and the spectrum was recorded in 40 fs, 250 fs and 1 ps time steps.

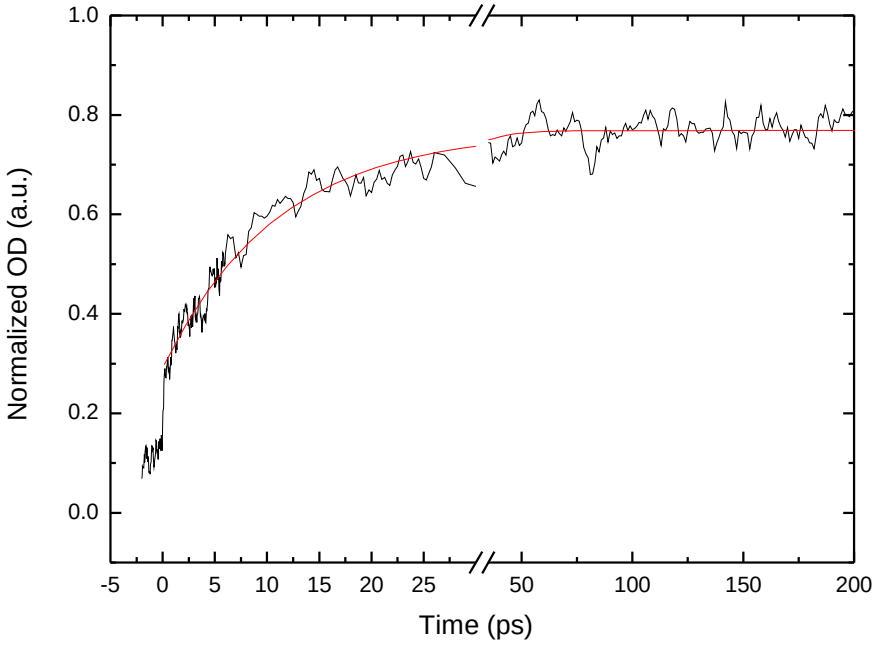

Figure 3.18: Temporal trace of the absorption signal of the electrons in the conduction band of the ZnO. The lineout was extracted from the transient absorption spectrum in Figure 3.17 at 2160 nm. The signal was found to rise with 200 fs, 2 ps and 10 ps.

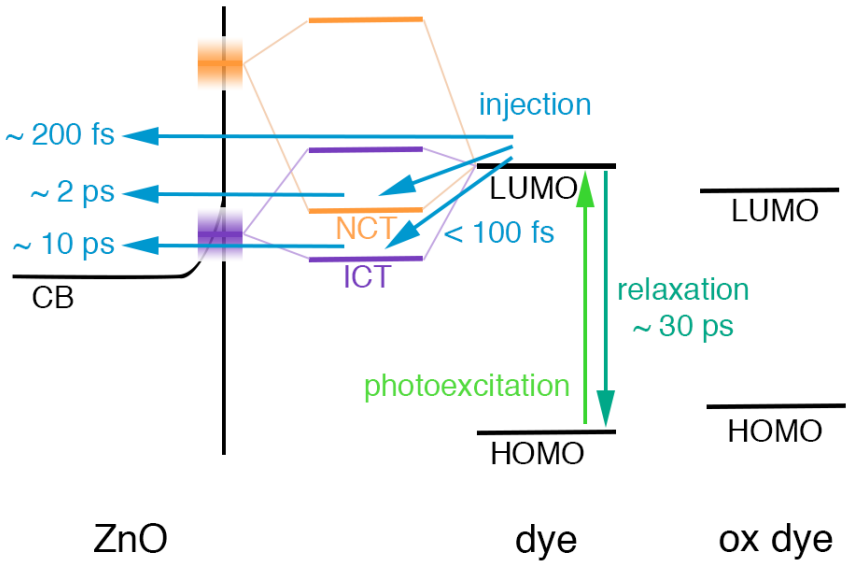

Figure 3.19: Schematic of the energy diagram of the DN216/ZnO DSSC with either spriOMeTAD or $I^-I_3^-$ as a hole conducting medium. Upon photoexcitation, electrons are injected from the LUMO of the dye to the conduction band (CB) of the ZnO leaving the dye oxidized. The injection of electrons into the CB of ZnO occurs either directly in 200 fs, via a neutral charge transfer state (NCT) in 2 ps or via an ionic charge transfer state (ICT). Injection via the charge transfer states are two-step processes where electrons are injected into either NCT or ICT and then into the CB of ZnO [1].

3.18. The absorption signal was fond to rise with three time constants: 200 fs, 2 ps and 10 ps.

Figure 3.19 summarizes the injection dynamics of electrons from the LUMO of the DN216 dye into the conduction band of ZnO, as detected by the newly developed pump near infrared transient absorption setup. After the excitation of the neutral dye, electrons are injected into the conduction band of ZnO either directly or via trap states at the surface between the dye and the semiconductor. Direct injection of electrons into the conduction band of ZnO was found to occur in 200 fs. Injection via surface trap state was found to be a two-step process; electrons are injected into the surface states in $<$100 fs and then into conduction band of ZnO in 2 ps and 10 ps.

The two decay constants of 2 ps and 10 ps are assigned to the neutral charge transfer state (NCT) and the ionic charge transfer state (ICT), respectively. These two charge transfer states result from the hybridization between the molecular orbitals of the dye and surface states of the ZnO at the interface between the two [1]. The injection into the trap states is beyond the temporal resolution of our setup ($<$ 200 fs). The injection of electrons from the NCT state, in 2 ps, was observed in the decay of the absorption signal in the spectral range 1500 - 2000 nm as shown in Figure 3.15. This decay constant was also detected in the rise of the absorption signal of the oxidised dye

[34]. The injection of electrons from the ICT state in 10 ps was observed in the decay of the absorption signal between 1000 nm and 1400 nm, as shown in Figure 3.13. Unlike the NCT state, the oxidised dye was already formed at the first injection into the ICT state therefore, the injection of electrons from the ICT state into the conduction band of ZnO was not reflected in the rise time of the oxidised dye.

4. Temporal Characterization of Femtosecond Near Infrared Pulses

The production of a transient absorption spectrum requires two femtosecond laser pulses, the pump to initiate charge dynamics within the sample and the probe pulse to scan the associated change in absorption spectra. The source of both the pump and the probe pulses in our laboratory, as described in Chapter 2, is a regenerative amplifier system that delivers pulses of 775 nm central wavelength and a duration of 150 fs. The pulse out of the laser undergoes wavelength conversion processes to produce a pump pulse of central wavelength corresponding to the maximum absorption of the sample and a probe pulse of a specific spectral window. Due to these wavelength conversion processes, the durations of the pump and the probe pulses become different to the original laser output pulse. Not only the pulse's spectral contents but also its duration is affected by normal dispersion, absorption and nonlinearity of the media it passes through. The temporal resolution of a pump-probe transient absorption spectroscopic measurement depends on the duration of both the pump and probe pulses. The characterization of the temporal profile of the pump and probe, as they propagate to the sample through various optical elements, is necessary to identify whether or not they fit the criteria of a high-resolution transient absorption spectrum.

In this work, a probe pulse of spectral window in the near infrared range (900 nm -2400 nm) has been generated by converting the central wavelength of the pulse out of the laser using a noncollinear optical parametric amplifier (NOPA). This chapter summarizes the results obtained from the temporal characterization of the generated pulses.

The challenge in detecting the temporal profile and phase of a femtosecond laser pulse lies in finding a detector that has a photoelectric response as fast as the duration of the pulse. Optical characterization techniques utilizing ultrashort pulses themselves as measurement tools have been developed to overcome this obstacle. The basis of these techniques is to convolve the laser pulse of unknown amplitude and phase with either its time-delayed replica or a pre-characterized reference pulse. The recorded convolution trace of the two pulses will then be deconvolved to retrieve the characteristics of the unknown pulse.

Second harmonic generation (SHG) autocorrelation is one of the simplest optical characterization techniques used to determine the duration of femtosecond pulses. In this method the correlation function is the intensity of the second harmonic resulting from the overlap of the pulse to be correlated and its time delayed copy. Assuming a specific pulse shape, the duration of the unknown pulse can be determined from the measured correlation function. This method provides no information about the phase of the pulse since it only measures its temporal profile. Moreover, the method requires the nonlinear frequency doubling crystal to be transparent to the second harmonic of the pulse to be measured, which is not the case for pulses in the UV range for example [39].

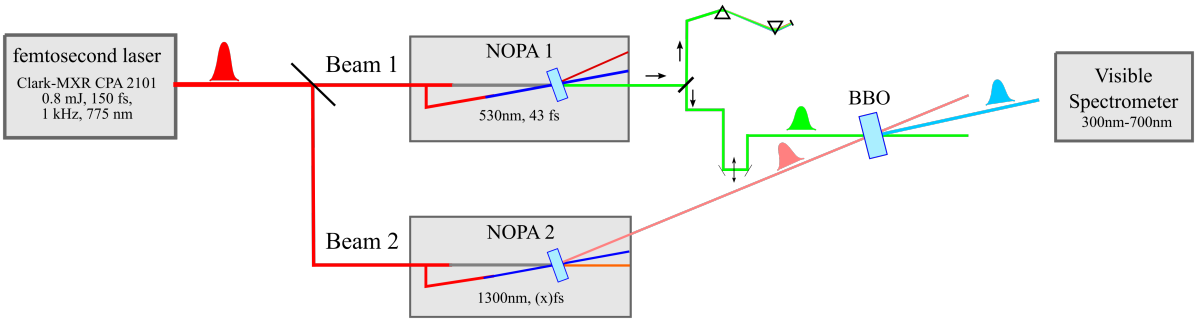

Figure 4.1: Schematic of the XFROG measurement setup.

Cross correlation frequency resolved optical gating (XFROG) is the optical characterization technique selected in this work to retrieve the phase and amplitude of the femtosecond near infrared pulses generated. The method was first introduced by Linden *et al.* [12, 39] to retrieve the amplitude and phase of weak pulses in the UV range. It is based on frequency mixing a reference pre-characterized pulse with the pulse to be retrieved (the unknown pulse) to produce a delay scan between the two pulses from which the phase and duration of the unknown pulse can be determined. This characterization technique was selected in this work because it allows for the determination of the duration and phase of the near infrared pulse with minimum adjustment to the existing pump probe transient absorption setup.

Figure 4.1 is a scheme of the XFROG experimental setup used to retrieve the duration and phase of the near infrared pulses. The output beam of the femtosecond laser, generating 150 fs short pulses of 775 nm central wavelength, is split into two beams labelled Beam 1 and Beam 2 in the figure. The reference beam is generated by tunning the central wavelength of Beam 1 to $\lambda_r = 530$ nm using the noncollinear optical parametric amplifier labelled NOPA 1 in the figure. The beam out of NOPA 1 is then sent to a two Brewster angle prism compressor to shorten the duration of its pulses to sub 50 fs. The reference beam then passes through two mirrors mounted on a mechanical translation stage on its way to a 3 mm Beta Barium Borate (BBO) crystal. By moving the stage backward (or forward) the optical path of the reference pulse can be lengthened (or shortened) and its arrival time to the BBO crystal with respect to the arrival time of the unknown pulse can be controlled. The central wavelength of Beam 2 is tuned to $\lambda_u = 1300$ nm using the idler of NOPA 2 before being sent to overlap spatially with the reference beam.

The temporal overlap between the reference (Beam 1) and the unknown (Beam 2) pulses is insured by adjusting the optical path of the reference pulse using the mechanical delay stage. As a result of the temporal and spatial overlap of the two beams a third beam of central wavelength $\lambda_t = 376$ nm is generated. Energy conservation requires the

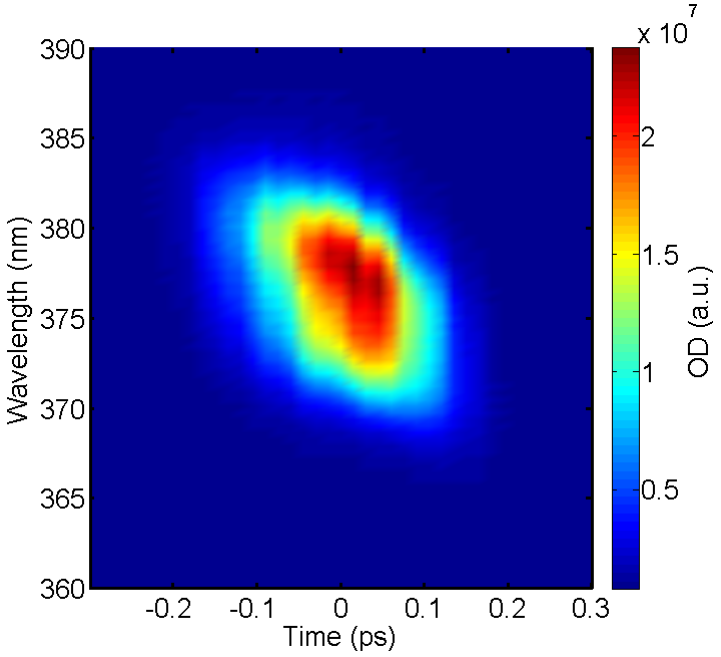

Figure 4.2: The XFROG trace obtained using a reference pulse of 530 nm central wavelength and an unknown pulse of 1300 nm central frequency.

following relation between the three beams:

$$\frac{hc}{\lambda_t} = \frac{hc}{\lambda_u} + \frac{hc}{\lambda_r}. \tag{4.1}$$

The resulting visible signal (shown as a blue line in Figure 4.1)is then sent to a visible spectrometer. A delay scan of the reference pulse to the unknown pulse is then recorded by moving the mechanical stage in steps of 15 fs. The XFROG trace recorded is shown in Figure 4.2; the delay between the reference and the unknown pulses on the x-axis, the wavelength on the y-axis and the optical density (OD) presented in arbitrary units as a color code. The details of the XFROG measurement and the analysis of the results obtained will be presented in section 4.2.

The spectrum of the reference pulse shown in Figure 4.3 was recorded using an optical fibre spectrometer (Ocean Optics USB series). The spectral width of the pulse in terms of wavelength is $\Delta\lambda = 11$ nm. For the duration of the reference pulse, an autocorrelation measurement was performed on the pulse. A brief introduction to the principles of autocorrelation and the results obtained is presented in the following section.

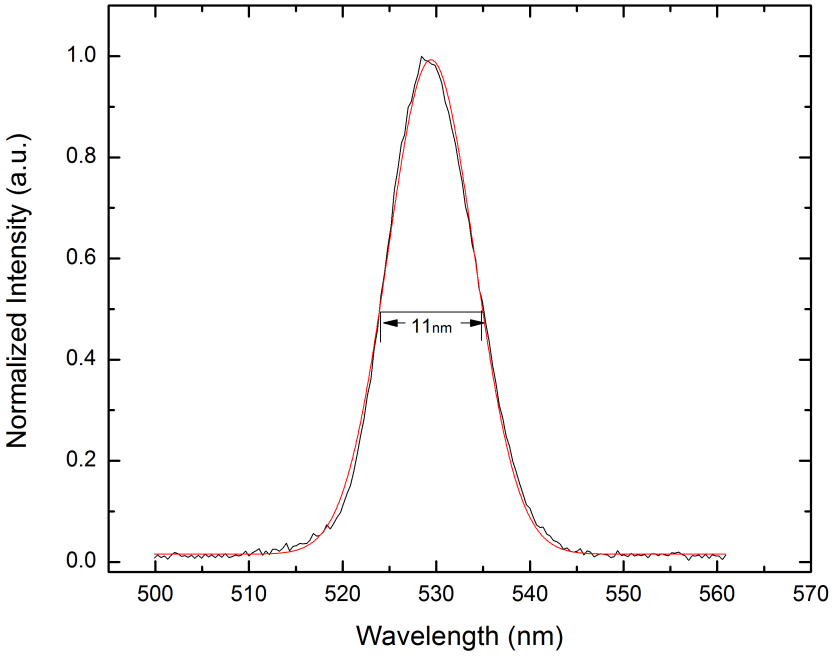

Figure 4.3: The spectrum of the reference pulse fitted with a Gaussian (red line): Central wavelength $\lambda = 530$ nm and the full width at half maximum $\Delta\lambda = 11$ nm.

4.1 Characterization of the Reference Pulse using Autocorrelation

The mathematical description of the autocorrelation function between two time-dependent functions $f(t)$ and $g(t)$ is given by:

$$A(T) = \int_{-\infty}^{+\infty} f(t)\, g(t-T)dt; \tag{4.2}$$

where T is the time delay between the two functions. Intensity autocorrelation is an optical setup that uses this well known mathematical principle to measure the duration of ultrashort laser pulses. The two time-dependent functions in intensity autocorrelation are the intensity of the electric fields of the pulse to be measured $I_1(t)$ and the intensity of its time delayed replica $I_2(t-T)$. In the experimental setup T is the delay between the arrival times at the detector of the two pulses due to the difference in optical path lengths.

Assuming a pulse of a Gaussian-shaped envelope, the intensity of the electric field of the pulse $I(t) \propto |E(t)|^2$ can be represented by:

$$I_1(t) = e^{\frac{-2t^2}{\tau_1^2}}; \tag{4.3}$$

where τ_1 is the duration of the pulse at $1/e$ of its electric field. As can be seen in the above expression the autocorrelation provides no information about the phase of the

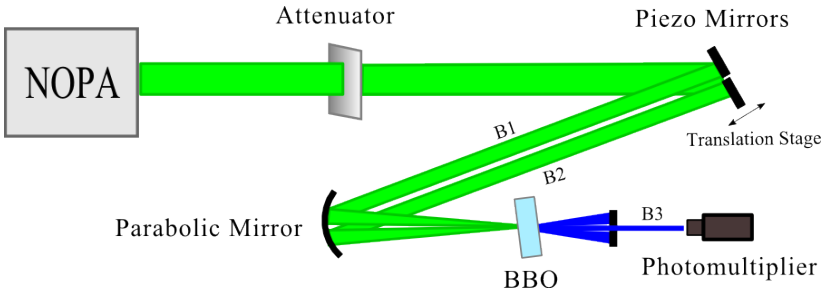

Figure 4.4: A schematic of the second harmonic generation (SHG) autocorrelator used to determine the duration of the reference pulse.

pulse. Similarly, the intensity of the electric field of the time delayed replica of the pulse is given by:

$$I_2(t-T) = e^{\frac{-2(t-T)^2}{\tau_2^2}}. \tag{4.4}$$

Therefore, the autocorrelation function will be:

$$\begin{aligned} A(T) &= \int_{-\infty}^{\infty} I_1(t)\, I_2(t-T)\, dt \\ &= \int_{-\infty}^{\infty} e^{\frac{-2t^2}{\tau_1^2}}\; e^{\frac{-2(t-T)^2}{\tau_2^2}}\, dt \\ &= e^{\frac{-2T^2}{\tau_2^2}} \int_{-\infty}^{\infty} e^{-(\frac{2}{\tau_1^2}+\frac{2}{\tau_2^2})t^2}\; e^{(\frac{4T}{\tau_2^2})t}\, dt. \end{aligned}$$

Using $\int_{-\infty}^{\infty} e^{-at^2}\, e^{bt} dt = \frac{\sqrt{\pi}}{\sqrt{a}}\, e^{\frac{b^2}{4a}}$ where $[Re(a) < 0]$, the above integral can be solved to give:

$$A(T) = \frac{\sqrt{\pi}}{\sqrt{\left(\frac{2}{\tau_1^2}+\frac{2}{\tau_2^2}\right)}}\, e^{-2\left[\frac{1}{\tau_2^2}-\frac{\tau_1^2}{\tau_2^2(\tau_1^2+\tau_2^2)}\right]T^2}. \tag{4.5}$$

This autocorrelation function is again a Gaussian function and the argument between the square brackets in the expression 4.5 is the reciprocal of its duration. Knowing that $\tau_1 = \tau_2 = \tau$, the relation between the duration τ_c of the autocorrelation function and the duration τ of the pulse is:

$$\tau_c = \sqrt{2}\, \tau. \tag{4.6}$$

In terms of the full width at half maximum:

$$\Delta t_c = \sqrt{2}\, \Delta t. \tag{4.7}$$

The autocorrelator setup used to measure the duration of the reference pulse is illustrated in Figure 4.4. The autocorrelation signal recorded is the second harmonic of the pulse to be measured with double the frequency 2ω. The input beam is sent through an attenuator to two adjacent D-shaped mirrors dividing it into two beams of equal intensities. To create the time delay (T) between the pulse and its replica, one of the

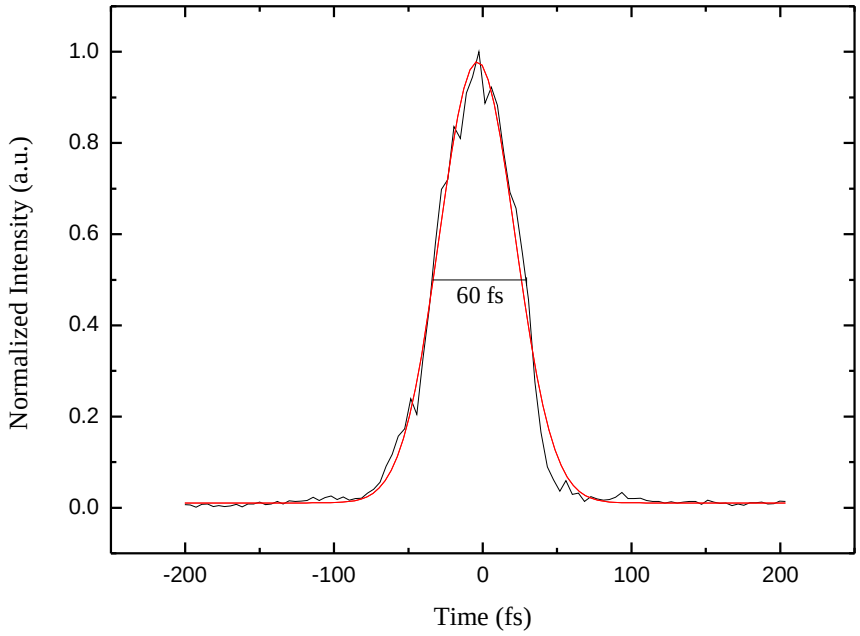

Figure 4.5: The reference pulse autocorrelation signal fitted with a Gaussian function (red line). The full width at half maximum of the fitting Gaussian is 60 fs.

two D mirrors is mounted on a piezoelectric translation stage that scans back and forth with respect to the other mirror.

The beams reflected of the two mirrors (B1 and B2 in the figure) are focused using a spherical mirror into a BBO crystal. The phase matching condition for generating the second harmonic of the two beams B1 an B2 is fulfilled by rotating the crystal around its optical axis. At the correct crystal orientation, two beams of frequency 2ω are generated along the same direction of B1 and B2 as well as a third beam (B3) along the optical axis of the crystal. Beam B3 is also the second harmonic of the input beam but was generated by the interaction of photons of B1 with photons B2 rather than photons of the same beam. The intensity of this beam is recorded by a photomultiplier synchronized with the motion of the motor of the mirror. An iris is placed behind the BBO crystal to ensure that only the beam B3 reaches the photomultiplier.

Figure 4.5 shows the autocorrelation trace recorded for a reference pulse as a function of the delay time (T). Fitting the trace with a Gaussian function, its full width at half maximum (FWHM) was found to be 60 fs. As explained in Equation 4.7 the duration Δt of the reference pulse is therefore 42 fs. As can be seen in Figure 4.3 the wavelength full width at half maximum of the reference pulse $\lambda_0 = 530$ nm was measured to be $\Delta\lambda = 11$ nm, therefore the duration-bandwidth product is:

$$\Delta t\ \Delta\omega = 2\pi\Delta t\ \Delta\nu = 2\pi\ 42 \times 10^{-15} \times 11 \times 10^{12} = 2\pi\ 0.462. \tag{4.8}$$

The calculated duration-bandwidth product is comparable to the theoretical value presented in Equation 2.2 ($\Delta t\ \Delta\omega = 2\pi\ 0.441$), therefore the assumption of a transform

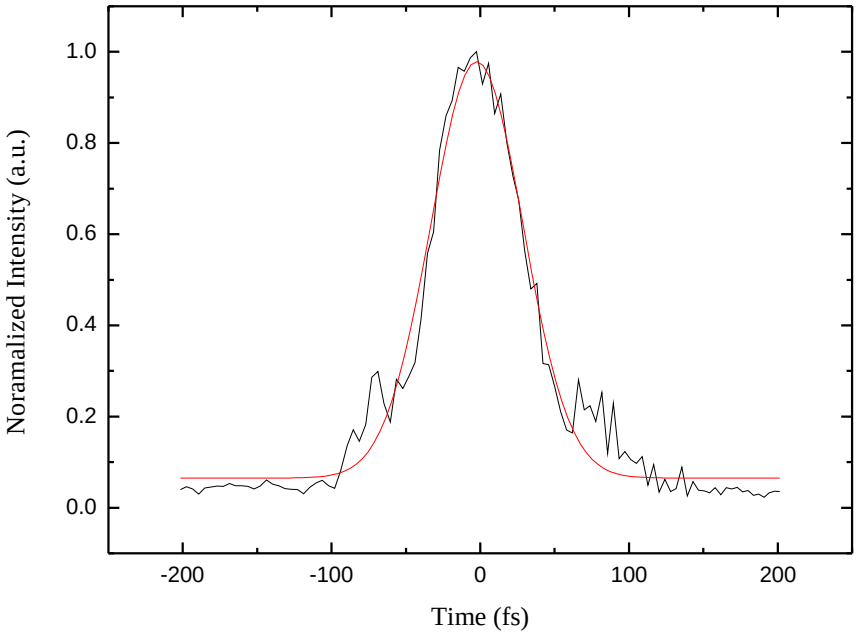

Figure 4.6: Autocorrelation trace of a reference pulse of central wavelength of 540 nm. The full width at half maximum of this signal is 73 fs indicating a duration of 51 fs for the reference pulse.

limited pulse is a valid one and the reference pulse has a constant phase.

Another reference pulse of central wavelength of $\lambda_r = 540$ nm was also used to determine the amplitude and phase of near infrared pulses of central wavelengths λ_{IR} of 1400, 1600 and 1900 nm. The duration of this reference pulse was determined to be 51 fs using autocorrelation. The autocorrelation trace for this pulse is shown in Figure 4.6. The spectral width of this pulse is $\Delta\lambda = 30$ nm.

4.2 Cross correlation Frequency Resolved Optical Gating

As mentioned before an XFROG measurement was performed by overlapping a reference pulse of 530 nm central wavelength in a BBO crystal with an infrared pulse of central wavelength of 1300 nm. In the original XFROG measurement introduced by Linden *et al.* [39] an algorithm was proposed to retrieve the amplitude and phase of the unknown pulse. In this work a simpler method was used to analyse the trace recorded. A horizontal lineout was extracted from the XFROG trace at the central wavelength $\lambda_t = 376$ nm predicted by Equation 4.1. This central lineout was then fitted with a Gaussian function, as illustrated in Figure 4.7, of $\Delta t = 157$ fs FWHM. The lineout is the convolution of the reference and the unknown pulse at 376 nm. Therefore, the

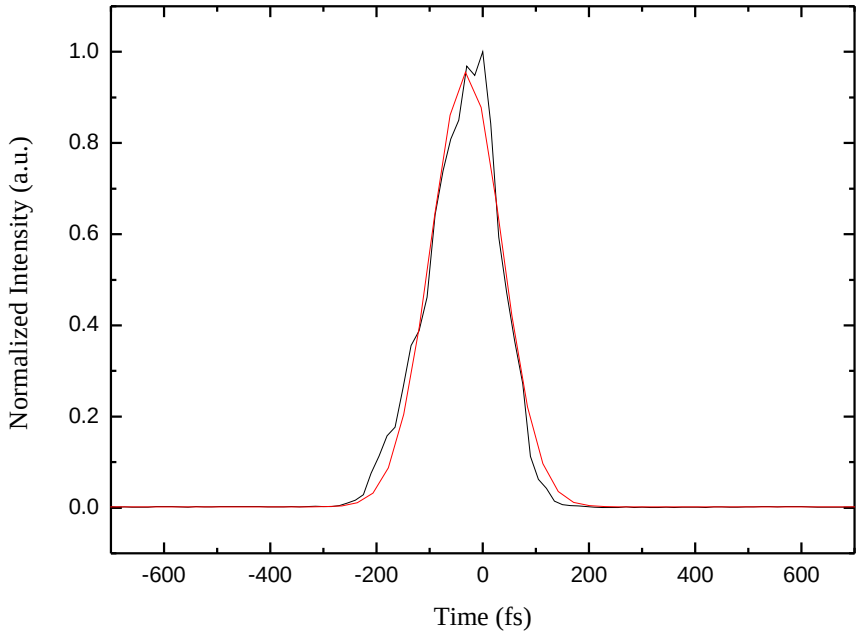

Figure 4.7: Horizontal lineout extracted from the XFROG trace shown in Figure 4.2 at 377 nm. The lineout was fitted with a Gaussian function and the duration $\Delta t = 157$ fs.

duration of the unknown pulse can be calculated as:

$$\Delta t_u = \sqrt{\Delta t_t^2 - \Delta t_r^2} = \sqrt{(157)^2 - (42)^2} = 151 \text{ fs}. \tag{4.9}$$

A number of horizontal lineouts were also extracted at wavelengths shorter and longer than the central wavelength to determine the chirp of the XFROG trace. Assuming a flat phase for the reference pulse the chirp seen in the XFROG trace is assigned to the unknown near infrared pulse. The arrival time of each of the spectral components with respect to the arrival time of the central spectral component i.e the chirp of the near infrared pulse is plotted in Figure 4.8. The chirp plotted in frequency domain is shown in Figure 4.9. Fitting the chirp with a linear fit and taking the slope, the chirp constant $C = \frac{d\omega}{dt} = 2\pi\frac{d\nu}{dt}$ introduced in Equation 2.5 was found to be 13×10^{26} s^{-2}.

A set of three other XFROG measurements were also performed using a reference pulse of central wavelength of $\lambda_r = 540$ nm to determine the duration of near infrared pulses of central wavelengths λ_{IR} of 1400, 1600 and 1900 nm. The XFROG traces are shown in Figure 4.10. An almost flat chirp can be seen in these three traces. This is attributed to the reduction in the changes in the value of the refractive index of the BBO crystal, where the pulses are generated [40].

Horizontal lineouts at the central wavelengths of 390 nm, 404 nm and 420 nm were extracted from the XFROG traces for the 1400 nm, 1600 nm and 1900 nm near infrared pulses, respectively. The lineouts were fitted with Gaussian functions, as shown if Figure 4.11 and the duration for each was determined. The results obtained from

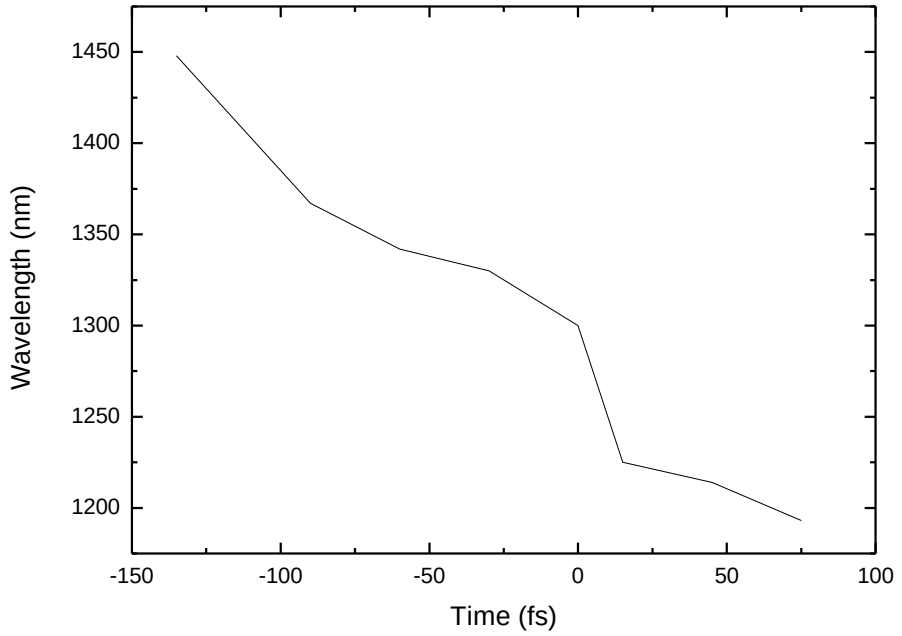

Figure 4.8: The chirp of a near infrared pulse centered at 1300 nm extracted from the XFROG trace 4.2.

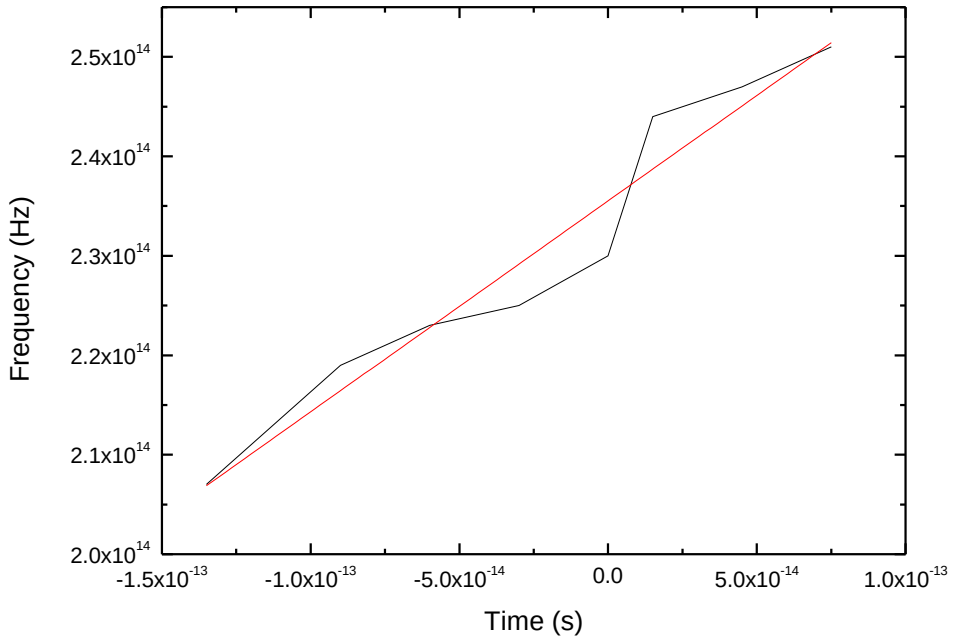

Figure 4.9: The chirp in frequency domain. The slope is 2.12×10^{26} s^{-2}.

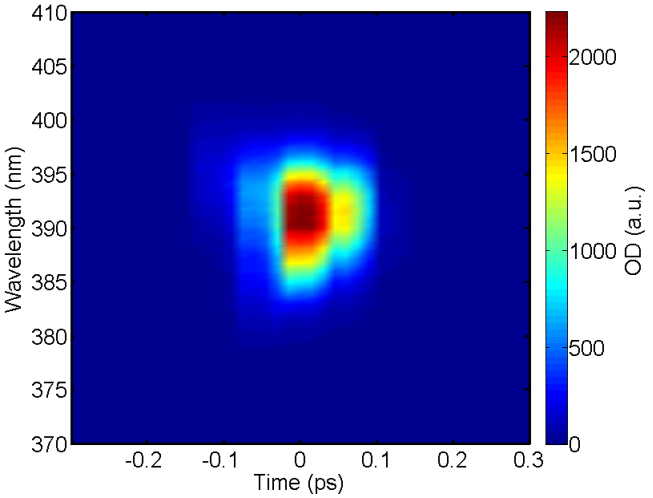

(a) 1400 nm

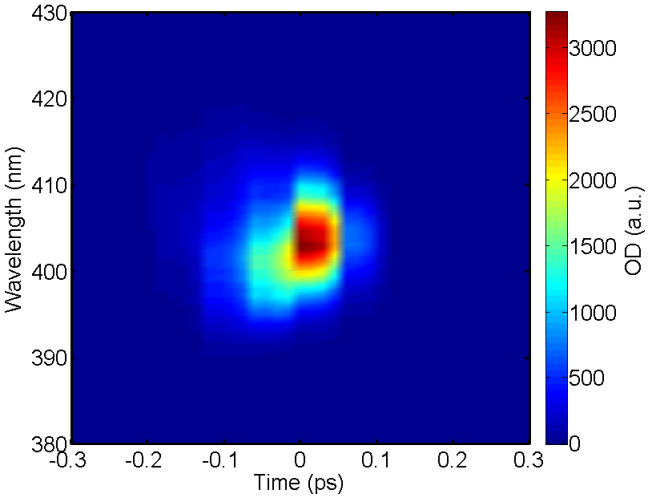

(b) 1600 nm

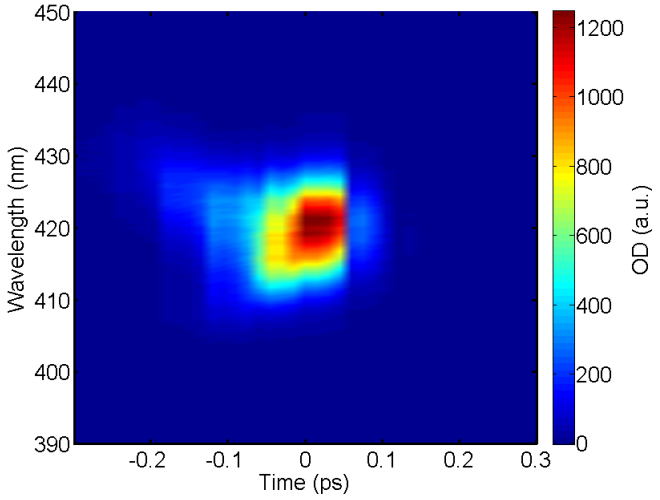

(c) 1900 nm

Figure 4.10: XFROG trace measured for a reference pulse of central wavelength of 540 nm and duration of 53 fs overlapped with an infrared pulse of central wavelength of 1400 nm.

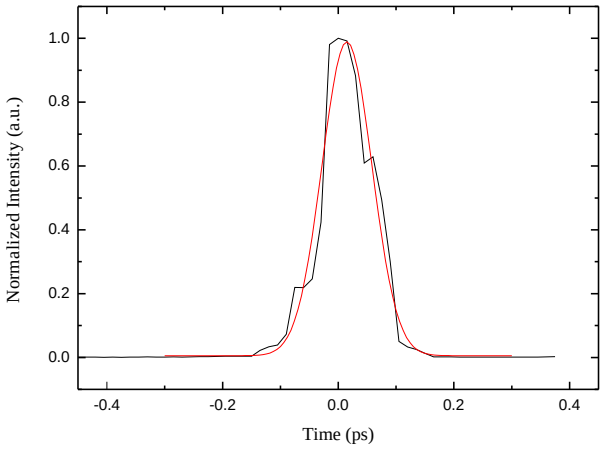

(a) 1400 nm

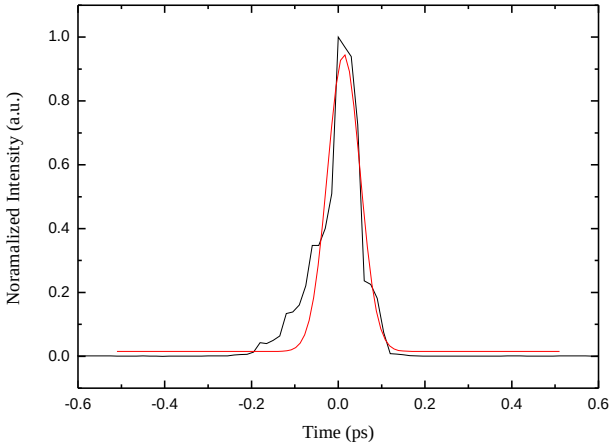

(b) 1600 nm

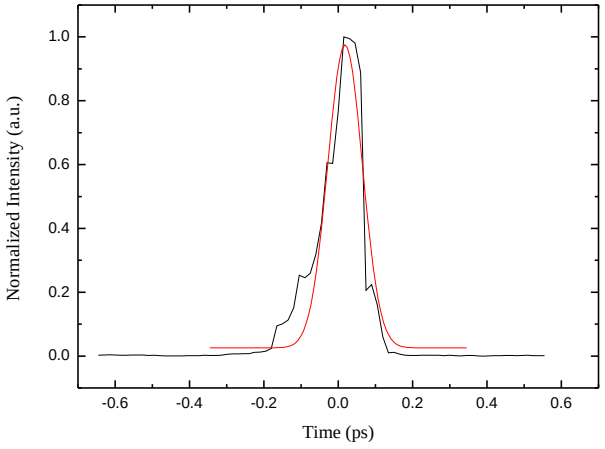

(c) 1900 nm

Figure 4.11: Horizontal lineouts extracted from the XFROG traces shown in Figure 4.10 at (a) 390 nm, (b) 404 nm, (c) 420 nm. The lineouts were fitted with Gaussian functions and the durations were found to be (a) 101 fs, (b) 88 fs, (c) 109 fs.

Table 4.1: A summary of the durations Δt_c extracted by taking horizontal lineouts at the central wavelengths λ_c and the corresponding durations of near infrared pulses Δt_{IR}.

λ_{IR} (nm)	λ_c (nm)	Δt_c (fs)	Δt_{IR} (fs)
1400	390	101	86
1600	404	88	70
1900	420	109	96

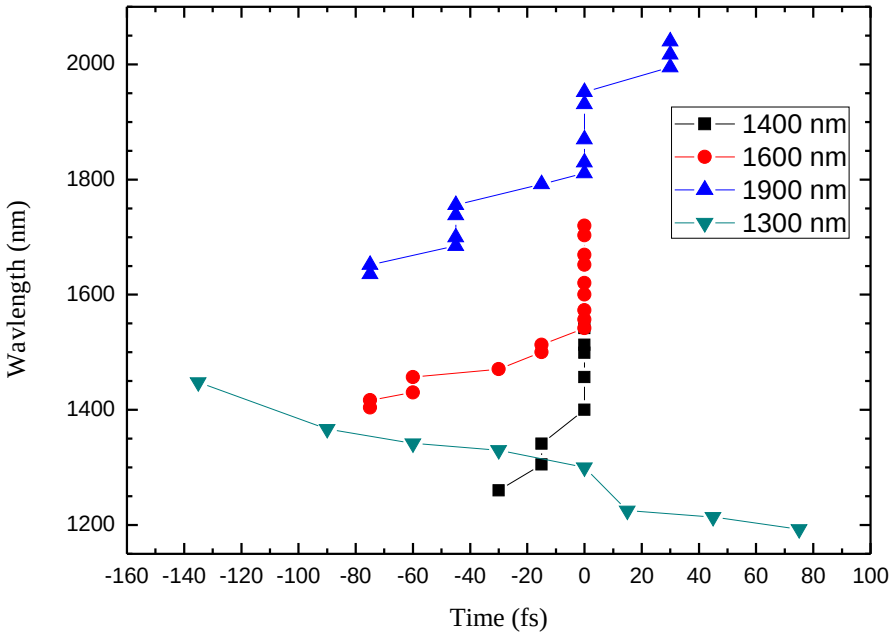

Figure 4.12: The chirp of near infrared pulses centered at 1400 nm, 1600 nm and 1900 nm extracted from the XFROG traces in Figure 4.10. The chirp of the pulse centered around 1300 nm was also included for comparison.

the fit and the calculated pulse durations are summarized in Table 4.1.

The retrieved chirp of the near infrered pulses centred around 1400 nm, 1600 nm and 1900 nm are presented in Figure 4.12 along with the chirp of the 1300 nm pulse. The negative chirp observed could be inherited from the reference pulse chirp.

5. Summary and Conclusion

Pump probe femtosecond transient absorption spectroscopy is an experimental technique to detect photophysical and photochemical processes in real time. This technique requires two femtosecond laser pulses, the pump to excite the sample and initiate charge dynamics, and the probe to scan the absorption of the sample's photoexcited molecules. Ideally, the source of the pump pulse must be of tunable wavelength to allow for the detection of photoinduced dynamics within samples of different excitation wavelength. The probe pulse's source must cover a broad spectral range to allow for the detection and comparison of various spectral signatures. Commercially available lasers are centred around one wavelength value, therefore require a frequency conversion technique to produce such pump and probe pulses. The laser in our laboratory is a regenerative Ti:Sa amplifier system (Clark MXR CPA 2101) that delivers pulses of central wavelength of 775 nm.

In this work, near infrared femtosecond probe pulses in the spectral range 900 - 2400 nm were generated using a noncollinear optical parametric amplifier (NOPA) pumped by the laser aiming for an extension to the existing probe spectral window. The amplitude and phase of exemplary near infrared pulses of central wavelength of 1300 nm, 1400 nm, 1600 nm and 1900 nm were retrieved using cross correlation frequency resolved optical gating (XFROG). The duration of the pulse centred around 1300 nm was found to be 151 fs and the chirp constant C is 13×10^{26} s^{-2}. The durations of the pulses centred around 1400 nm, 1600 nm and 1900 nm were measured to be 86 fs, 70 fs and 96 fs. The three later pulses showed a less pronounced chirp than the pulse around 1300 nm which was attributed to the decrease in the change in the refractive index of the BBO crystal as the wavelength increase [40].

The near infrared idler pulses were used as a probe source to investigate the charge dynamics within organic solar cells using the transient absorption setup presented in Chapter 2. Two types of solar cells were investigated, Indoline dye sensitized solar cells utilizing zinc oxide (ZnO) as a semiconductor and fluorinated zinc phthalocyanine F_nZnPc/C_{60} ($n = 0, 4, 8, 16$) bilayer photovoltaic cells.

In the DN216/ZnO dye sensitized solar cell, the light absorber was an indoline dye that injected electrons into the conduction band of the ZnO semiconductor upon photoexcitation. Injection of electrons into the semiconductor's conduction band was found to occur either directly, via a neutral charge transfer state (NCT), or via ionic charge transfer state (ICT). The direct injection of electrons takes place on an ultrafast time scale of about 200 fs. It was observed from the rise of the absorption signal at $>$ 2000 nm - 2400 nm of the conduction band of ZnO. This signal was also found to rise in about 2 ps and 10 ps. The rise of the absorption signal in 2 ps was attributed to the electrons injected from the NCT state. This assignment was confirmed by the decay of absorption of this charge transfer state in the range 1500 nm - 2000 nm with the same time constant. Similarly, the rise of of the signal in 10 ps was assigned to ICT state

and was confirmed by the decay in its absorption in the spectral range 1000 nm - 1400 nm.

As for the F_nZnPc/C_{60} ($n = 0, 4, 8, 16$) cells the fluorinated zinc phthalocyanines that acts as the electron donor, and the C_{60} which is the electron acceptor are both light absorbers. The injection of electrons from the donor into the organic semiconductor occurs after the dissociation of excitons, coulombically bound electron hole pairs, at the donor/acceptor heterojunction. The energetics at this interface affects the dissociation of excitons and the subsequent creation of free charge carriers [2]. After excitation of C_{60} a C_{60}^- anion is created due to autoionization, a process by which an electron is transferred from the excited C_{60} molecule to a neighbouring molecule [30]. Excitation of the C_{60} can occur either by direct absorption of photons or by the injection of the electrons from the fluorinated phthalocyanines. In all four fluorinated cells, the absorption of the C_{60}^- anion was found to appear instantaneously indicating that autoionization is independent of the energetics at the donor/acceptor heterojunction. It was also found that the absorption signal in all F_nZnPc/C_{60} ($n = 0, 4, 8, 16$) cells decays with two time constants: a short time constant of 3 ps,4 ps, 4 ps and 5 ps attributed to recombination within the bulk of the C_{60} layer whereas the long time decay of 34 ps, 52 ps, 37 ps, 45 ps, respectively, was assigned to the recombination at the surface of the C_{60} layer with air.

The investigation of the charge dynamics occurring within ZnO, which is the semiconductor in the indoline dye sensitized solar cell presented in this work was not possible without the extension of the probe window to the near infrared range using the newly developed source. The improved temporal resolution of the TAS setup using this source also allowed for the comparison of the speed by which the creation of the C_{60}^- anion in the four fluorinated cells F_nZnPc/C_{60} ($n = 0, 4, 8, 16$) occur, therefore, giving a more detailed view of the microscopic effects that gradual fluorination has on them.

Appendix

Propagation of Ultrashort Pulses in Optically Transparent Media

An ultrashort pulse propagating through a dielectric medium experiences a duration broadening, a delay and a phase shift [14]. This is attributed to the broad spectral content of the pulse and the variation between the propagation speed of each its spectral components. To illustrate how this conclusion was driven, let us consider the description of the electric field of an ultrashort laser pulse as it propagates a distance x through the medium:

$$E(\omega, x) = e^{\frac{-(\omega-\omega_0)^2}{4/\tau^2}} e^{-ikx}, \tag{1}$$

where k, the propagation factor is a function of the the frequency. This factor can be Taylor expanded around the central frequency ω_0 as:

$$k(\omega) = k(\omega_0) + k'(\omega_0)(\omega - \omega_0) + \frac{1}{2}k''(\omega_0)(\omega - \omega_0)^2 + ... \tag{2}$$

Substituting 2 into 1 we obtain the following value for the electric field:

$$\begin{aligned} E(\omega, x) &= e^{(\frac{-(\omega-\omega_0)^2}{4/\tau^2})} \quad e^{(-i(k+k'(\omega-\omega_0)+\frac{1}{2}k''(\omega-\omega_0)^2)x)} \\ &= e^{(\frac{-\tau^2}{4}(\omega^2-2\omega_0\omega+\omega_0^2)-ikx-ik'\omega x+ik'\omega_0 x-\frac{i}{2}k''x(\omega^2-2\omega_0\omega+\omega_0^2))} \\ &= e^{(\frac{-\tau^2}{4}\omega^2+\frac{\tau^2}{2}\omega_0\omega-\frac{\tau^2}{4}\omega_0^2-ikx-ik'\omega x+ik'\omega_0 x-\frac{i}{2}k''x\omega^2+ik''\omega_0\omega x-\frac{i}{2}k''x\omega_0^2)} \\ &= e^{(-ikx+ik'\omega_0 x-\omega_0^2(\frac{\tau^2}{4}+\frac{i}{2}k''x))} \quad e^{(\frac{\tau^2}{2}\omega_0\omega-ik'\omega x+ik''\omega_0\omega x-\omega^2(\frac{\tau^2}{4}+\frac{i}{2}k''x))}. \end{aligned} \tag{3}$$

For simplicity we introduce the factor $\Gamma(x)$ defined by:

$$\frac{1}{\Gamma(x)} = \tau^2 + 2ik''x \tag{4}$$

Now, the electric field in terms of $\Gamma(x)$ will be:

$$E(\omega, x) = e^{-ikx+ik'\omega_0 x-\frac{\omega_0^2}{4\Gamma(x)}} e^{(\frac{\tau^2}{2}\omega_0+ik''\omega_0 x-ik'x)\omega} e^{\frac{-1}{4\Gamma(x)}\omega^2} \tag{5}$$

The electric field of the pulse as a function of time can be obtained by inverse Fourier transform the above expression:

$$\begin{aligned} E(t, x) &= \frac{1}{2\pi}\int_{-\infty}^{\infty} E(\omega, x)e^{i\omega t}d\omega \\ &= \frac{1}{2\pi}e^{-ikx+ik'\omega_0 x-\frac{\omega_0^2}{4\Gamma(x)}}\int_{-\infty}^{\infty} e^{(\frac{\omega_0}{2\Gamma(x)}+i(t-k'x))\omega} e^{\frac{-1}{4\Gamma(x)}\omega^2}d\omega. \end{aligned} \tag{6}$$

Using $\int_{\infty}^{\infty} e^{ax}e^{bx^2}dx = \frac{\sqrt{\pi}}{\sqrt{-b}}e^{-\frac{a^2}{4b}}; Re[b] < 0$ the integral in Equation (6) can be solved and the electric field will then be:

$$\begin{aligned} E(t,x) &= \sqrt{\frac{\Gamma(x)}{\pi}}e^{-ikx+ik'\omega_0 x-\frac{\omega_0^2}{4\Gamma(x)}+\Gamma(x)(\frac{\omega_0}{2\Gamma(x)}+i(t-k'x))^2} \\ &= \sqrt{\frac{\Gamma(x)}{\pi}}e^{-ikx+ik'\omega_0 x-\frac{\omega_0^2}{4\Gamma(x)}+\Gamma(x)\frac{\omega_0^2}{4\Gamma^2(x)}+i\omega_0(t-k'\omega)-\Gamma(x)(t-k'x)^2} \\ &= \sqrt{\frac{\Gamma(x)}{\pi}}e^{i\omega_0(t-\frac{x}{\omega_0/k})}e^{-\Gamma(x)(t-k'x)^2} \end{aligned} \tag{7}$$

For further simplification we define the two velocities; the velocity of the composing plane waves i.e the phase velocity $v_\phi = \frac{\omega_0}{k}$ and the group velocity $v_g = \frac{d\omega}{dk}$. Now the electric field of the pulse will be:

$$E(t,x) = \sqrt{\frac{\Gamma(x)}{\pi}}e^{i\omega_0(t-\frac{x}{v_\phi})}e^{-\Gamma(x)(t-\frac{x}{v_g})^2} \tag{8}$$

Separating the real and imaginary parts of Equation (4), $\Gamma(x)$ can be written as:

$$\Gamma(x) = \frac{1/\tau^2}{1+\frac{4}{\tau^4}(k'')^2x^2} - i\frac{\frac{2}{\tau^2}k''x}{1+\frac{4}{\tau^4}(k'')^2x^2} \tag{9}$$

Substituting Equation (9) into Equation (8):

$$E(t,x) = Ae^{i\omega_0\left(t-\frac{x}{v_\phi}\right)}e^{\frac{1/\tau^2}{1+\frac{4}{\tau^4}(k'')^2x^2}\left(t-\frac{x}{v_g}\right)^2}e^{i\frac{\frac{2}{\tau^2}k''x}{1+\frac{4}{\tau^4}(k'')^2x^2}\left(t-\frac{x}{v_g}\right)^2}; \tag{10}$$

where $A = \frac{1}{\sqrt{\pi}}\sqrt{\frac{1/\tau^2}{1+\frac{4}{\tau^4}(k'')^2x^2} - i\frac{\frac{2}{\tau^2}k''x}{1+\frac{4}{\tau^4}(k'')^2x^2}}$.

The first exponent on the expression above shows that after propagating a distance x through the medium, the temporal relation between the central frequency ω_0 and the other spectral components of the pulse is shifted by x/v_ϕ. The second exponent shows that the pulse maintain its Gaussian shape but with broader temporal width(duration). We can also note that the envelope is delayed by x/v_g. Finally, the phase in the third exponent is quadratic and that is the origin of the linear frequency chirp.

Bibliography

[1] Minda, I., Ahmed, E., Sleziona, V., Richter, C., Beu, M., Falgenhauer, J., Miura, H., Schlettwein, D. and Schwoerer, H.: Identification of different pathways of electron injection in dye-sensitised solar cells of electrodeposited zno using an indoline sensitiser. *Physical Chemistry Chemical Physics*, vol. 18, no. 13, pp. 8938–8944, 2016.

[2] Brendel, M., Krause, S., Steindamm, A., Topczak, A.K., Sundarraj, S., Erk, P., Höhla, S., Fruehauf, N., Koch, N. and Pflaum, J.: The effect of gradual fluorination on the properties of fnznpc thin films and fnznpc/c60 bilayer photovoltaic cells. *Advanced Functional Materials*, vol. 25, no. 10, pp. 1565–1573, 2015.

[3] Hölzle, U.: Powering a google search. `https://googleblog.blogspot.co.za/2009/01/powering-google-search.html`, 2009.

[4] Claims for solar cell efficiency put to test at nrel. `http://www.nrel.gov/news/features/2016/21635`, . Accessed: 2016-08-31.

[5] Best research cell efficincies, national renewable energy laboratory(nrel). `http://www.nrel.gov/ncpv/images/efficiency_chart.jpg`, . Accessed: 2016-08-10.

[6] Brabec, C.J., Gowrisanker, S., Halls, J.J., Laird, D., Jia, S. and Williams, S.P.: Polymer–fullerene bulk-heterojunction solar cells. *Advanced Materials*, vol. 22, no. 34, pp. 3839–3856, 2010.

[7] Rumer, J.W. and McCulloch, I.: Organic photovoltaics: Crosslinking for optimal morphology and stability. *Materials Today*, vol. 18, no. 8, pp. 425–435, 2015.

[8] Hoppe, H. and Sariciftci, N.S.: Organic solar cells: An overview. *Journal of Materials Research*, vol. 19, no. 07, pp. 1924–1945, 2004.

[9] Schwoerer, M. and Wolf, H.C.: *Organic molecular solids*. John Wiley & Sons, 2007.

[10] Grätzel, M.: Solar energy conversion by dye-sensitized photovoltaic cells. *Inorganic chemistry*, vol. 44, no. 20, pp. 6841–6851, 2005.

[11] Wilhelm, T., Piel, J. and Riedle, E.: Sub-20-fs pulses tunable across the visible from a blue-pumped single-pass noncollinear parametric converter. *Optics letters*, vol. 22, no. 19, pp. 1494–1496, 1997.

[12] Linden, S., Giessen, H. and Kuhl, J.: Xfrog - a new method for amplitude and phase characterization of weak ultrashort pulses. *physica status solidi (b)*, vol. 206, no. 1, pp. 119–124, 1998.

[13] Diels, J.C. and Rudolph, W.: *Ultrashort laser pulse phenomena*. Academic press, 2006.

[14] Rullier, C.: *Femtosecond Laser Pulses.* Springer, 2005.

[15] Alfano, R. and Shapiro, S.: Observation of self-phase modulation and small-scale filaments in crystals and glasses. *Physical Review Letters*, vol. 24, no. 11, p. 592, 1970.

[16] Boyd, R.W.: *Nonlinear optics.* Academic press, 2003.

[17] Brodeur, A., Chien, C., Ilkov, F., Chin, S., Kosareva, O. and Kandidov, V.: Moving focus in the propagation of ultrashort laser pulses in air. *Optics Letters*, vol. 22, no. 5, pp. 304–306, 1997.

[18] Brodeur, A. and Chin, S.: Ultrafast white-light continuum generation and self-focusing in transparent condensed media. *JOSA B*, vol. 16, no. 4, pp. 637–650, 1999.

[19] Fork, R., Martinez, O. and Gordon, J.: Negative dispersion using pairs of prisms. *Optics letters*, vol. 9, no. 5, pp. 150–152, 1984.

[20] Martinez, O., Gordon, J. and Fork, R.: Negative group-velocity dispersion using refraction. *JOSA A*, vol. 1, no. 10, pp. 1003–1006, 1984.

[21] *Prism Compressor for Ultrashort Laser Pulses, Application Note 29.* Newport Corporation, Technology and Aplication Center, Newport Corporation, Worldwide Headquarters, 1791 Deere Avenue, Irvine, CA 92606, 2006.
Available at: `assets.newport.com/webDocuments-EN/images/12243.PDF`

[22] Chang, A.Y., Chen, Y.-H., Lin, H.-W., Lin, L.-Y., Wong, K.-T. and Schaller, R.D.: Charge carrier dynamics of vapor-deposited small-molecule/fullerene organic solar cells. *Journal of the American Chemical Society*, vol. 135, no. 24, pp. 8790–8793, 2013.

[23] Tang, C.W.: Two-layer organic photovoltaic cell. *Applied Physics Letters*, vol. 48, no. 2, pp. 183–185, 1986.

[24] Opitz, A., Ecker, B., Wagner, J., Hinderhofer, A., Schreiber, F., Manara, J., Pflaum, J. and Brütting, W.: Mixed crystalline films of co-evaporated hydrogen-and fluorine-terminated phthalocyanines and their application in photovoltaic devices. *Organic Electronics*, vol. 10, no. 7, pp. 1259–1267, 2009.

[25] O'Regan, B. and Grätzel, M.: A low-cost, high-efficiency solar cell based on dye-sensitized. *Nature*, vol. 353, no. 6346, pp. 737–740, 1991.

[26] Grätzel, M.: Photoelectrochemical cells. *Nature*, vol. 414, no. 6861, pp. 338–344, 2001.

[27] Mayer, T., Weiler, U., Kelting, C., Schlettwein, D., Makarov, S., Wöhrle, D., Abdallah, O., Kunst, M. and Jaegermann, W.: Silicon–organic pigment material hybrids for photovoltaic application. *Solar Energy Materials and Solar Cells*, vol. 91, no. 20, pp. 1873–1886, 2007.

[28] Meiss, J., Merten, A., Hein, M., Schuenemann, C., Schäfer, S., Tietze, M., Uhrich, C., Pfeiffer, M., Leo, K. and Riede, M.: Fluorinated zinc phthalocyanine as donor for efficient vacuum-deposited organic solar cells. *Advanced Functional Materials*, vol. 22, no. 2, pp. 405–414, 2012.

[29] Krause, S., Casu, M., Schöll, A. and Umbach, E.: Determination of transport levels of organic semiconductors by ups and ips. *New Journal of Physics*, vol. 10, no. 8, p. 085001, 2008.

[30] Lane, P.A., Cunningham, P.D., Melinger, J.S., Kushto, G.P., Esenturk, O. and Heilweil, E.J.: Photoexcitation dynamics in films of c 60 and zn phthalocyanine with a layered nanostructure. *Physical review letters*, vol. 108, no. 7, p. 077402, 2012.

[31] Lawson, D.R., Feldheim, D.L., Foss, C.A., Dorhout, P.K., Elliott, C.M., Martin, C.R. and Parkinson, B.: Near-ir absorption spectra for the buckminsterfullerene anions: an experimental and theoretical study. *Journal of The Electrochemical Society*, vol. 139, no. 7, pp. L68–L71, 1992.

[32] Brendel, M.: *Correlation between Interface Energetics of Molecular Semiconductors and Opto-Electronic Properties of Planar Organic Solar Cells*. Ph.D. thesis, Julius-Maxmilians-Universität, 2016.

[33] Kuik, M., Koster, L., Wetzelaer, G. and Blom, P.: Trap-assisted recombination in disordered organic semiconductors. *Physical review letters*, vol. 107, no. 25, p. 256805, 2011.

[34] Rohwer, E., Minda, I., Tauscher, G., Richter, C., Miura, H., Schlettwein, D. and Schwoerer, H.: Ultrafast charge-transfer reactions of indoline dyes with anchoring alkyl chains of varying length in mesoporous zno solar cells. *ChemPhysChem*, vol. 16, no. 5, pp. 943–948, 2015.

[35] Minda, I.: *Photoinduced charge dynamics in indoline-dye sensitised solar cells*. Master's thesis, Stellenbosch University, 2014.

[36] Falgenhauer, J., Richter, C., Miura, H. and Schlettwein, D.: Stable sensitization of zno by improved anchoring of indoline dyes. *ChemPhysChem*, vol. 13, no. 12, pp. 2893–2897, 2012.

[37] Bach, U., Lupo, D., Comte, P., Moser, J., Weissörtel, F., Salbeck, J., Spreitzer, H. and Grätzel, M.: Solid-state dye-sensitized mesoporous tio2 solar cells with high photon-to-electron conversion efficiencies. *Nature*, vol. 395, no. 6702, pp. 583–585, 1998.

[38] Furube, A., Katoh, R., Yoshihara, T., Hara, K., Murata, S., Arakawa, H. and Tachiya, M.: Ultrafast direct and indirect electron-injection processes in a photoexcited dye-sensitized nanocrystalline zinc oxide film: the importance of exciplex intermediates at the surface. *The Journal of Physical Chemistry B*, vol. 108, no. 33, pp. 12583–12592, 2004.

[39] Linden, S., Kuhl, J. and Giessen, H.: Amplitude and phase characterization of weak blue ultrashort pulses by downconversion. *Optics letters*, vol. 24, no. 8, pp. 569–571, 1999.

[40] Zhang, D., Kong, Y. and Zhang, J.-y.: Optical parametric properties of 532-nm-pumped beta-barium-borate near the infrared absorption edge. *Optics communications*, vol. 184, no. 5, pp. 485–491, 2000.